

Natural Realization of Tens-of-GeV Dark Matter in the GNMSSM

Fei Li^a, Junjie Cao^{a,b,*}

^a School of Physics, Henan Normal University, Xinxiang 453007, China

^b School of Physics, Zhengzhou University, Zhengzhou 450000, China

E-mail: hnufeili@163.com, junjiec@alumni.itp.ac.cn

ABSTRACT: This study presents a comparative analysis of the Minimal Supersymmetric Standard Model (MSSM), the Z_3 -symmetric Next-to-Minimal Supersymmetric Standard Model (Z_3 -NMSSM), and the General Next-to-Minimal Supersymmetric Standard Model (GNMSSM), incorporating constraints from dark matter (DM) relic density, the LUX-ZEPLIN 2024 experiment (LZ 2024), Higgs data, and the Large Hadron Collider (LHC). The results suggest that, among the three frameworks, only GNMSSM can naturally accommodate for light DM with a mass below 100 GeV. As such, the viable supersymmetry candidate is primarily Singlino-like. One key advantage of the GNMSSM is the effective decoupling between interactions that establish the relic density and those that control direct detection, allowing the model to satisfy all current experimental bounds simultaneously. We further explore two characteristic mass hierarchies in the GNMSSM parameter space, each exhibiting distinct phenomenological behaviors. The first hierarchy, $\tilde{S} < \tilde{B} < \tilde{H}$ (Singlino–Bino–Higgsino), involves a relatively light Bino and allows the Higgsino mass parameter, μ_{tot} , to be as low as about 200 GeV, naturally yielding light DM at tens of GeV. The dominant annihilation channels are then $\tilde{\chi}_1^0 \tilde{\chi}_1^0 \rightarrow A_s A_s$ in the h_1 scenario and $\tilde{\chi}_1^0 \tilde{\chi}_1^0 \rightarrow h_s A_s$ in the h_2 scenario, where h_s and A_s denote singlet-dominated CP-even and CP-odd Higgs bosons, respectively. The second hierarchy, $\tilde{S} < \tilde{H} < \tilde{B}$, corresponds to a heavy Bino. In this case, although the DM phenomenology remains qualitatively similar, LHC constraints require $\mu_{\text{tot}} \gtrsim 900$ GeV, implying a significant degree of fine-tuning in reproducing the Z -boson mass.

*Corresponding author.

Contents

1	Introduction	1
2	SUSY predictions of light DM	2
2.1	MSSM	2
2.2	Z_3 -NMSSM	5
2.3	GNMSSM	8
3	Comprehensive study of GNMSSM	9
3.1	Research strategy	10
3.2	Numerical results	13
3.3	Subtleties of LHC restrictions	19
4	Conclusion	23

1 Introduction

Among numerous dark matter (DM) candidates, Weakly Interacting Massive Particles (WIMPs) have long been favored by theorists due to their natural ability to produce the observed cosmic abundance through the thermal freeze-out mechanism [1]. According to this mechanism, WIMPs should interact with ordinary matter at a well-defined strength, yielding characteristic cross-sections: $\sim 10^{-45} \text{ cm}^2$ for spin-independent (SI) nucleon scattering [2] and $\sim 10^{-40} \text{ cm}^2$ for spin-dependent (SD) interactions [3]. However, direct detection experiments, particularly LUX-ZEPLIN 2024 (LZ 2024) [4], have pushed these upper limits down to 10^{-48} cm^2 and 10^{-43} cm^2 , respectively, posing substantial challenges for conventional WIMP models. To naturally resolve this tension, recent research has increasingly focused on extensions of economical WIMP theories by constructing DM structures that are nearly decoupled from the Standard Model (SM), leading to so-called “Secluded dark matter” models [5].

Cosmological measurements of effective light neutrino numbers and theoretical unitarity constraints place WIMPs within a broad mass range of 3.5 MeV [6] to 100 TeV [7, 8]. Within this window, the tens-of-GeV regime deserves special scrutiny for four reasons:

- Many DM theories link DM to electroweak symmetry breaking, providing theoretical motivation for DM at the electroweak scale [9, 10].

- Direct detection experiments reach their highest sensitivity in this mass range [4]. Thus, understanding how a WIMP can evade current bounds is invaluable for model building.
- Achieving the correct relic density often requires additional new particles with masses close to that of the WIMP. As such, establishing whether such states can elude Large Hadron Collider (LHC) searches is a key model-building constraint [9–11].
- Most critically, after accounting for current experimental limits, many theories face severe fine-tuning problems when predicting DM in this mass range (see the discussion below). Should future experiments confirm DM in this region, a number of theoretical frameworks would face fundamental challenges. Therefore, systematically exploring models that naturally predict DM in this range, and distinguishing them from other theoretical frameworks, constitutes an important research direction at the intersection of particle physics and cosmology.

As one of the most compelling physical models beyond the SM, supersymmetry (SUSY) naturally accommodates WIMP DM [1]. Consequently, studying tens-of-GeV DMs within supersymmetric frameworks has attracted considerable attention [12–15]. This paper systematically compares the Minimal Supersymmetric Standard Model (MSSM) [16, 17] and the Next-to-Minimal Supersymmetric Standard Model with Z_3 symmetry (Z_3 -NMSSM) [18, 19], highlighting their characteristics and differences for predicting DM of several tens of GeV. We further demonstrate how the General NMSSM (GNMSSM) can predict a much richer spectrum of DM phenomena and discuss implications for future experiments.

The remainder of this paper is organized as follows. Section 2 highlights the similarities and differences between the MSSM, the Z_3 -NMSSM, and the GNMSSM, in the context of attempts to realize a DM mass of $\mathcal{O}(10 \text{ GeV})$. In this process, the first two models are demonstrated to suffer from severe fine-tuning issues, while the GNMSSM avoids this problem. Section 3 then focuses on the GNMSSM, examining in detail how it produces a viable tens-of-GeV DM compatible with all current constraints. Conclusions are then summarized in Section 4.

2 SUSY predictions of light DM

2.1 MSSM

In the MSSM, a compelling DM candidate in the tens-of-GeV mass range is the lightest neutralino, which is predominantly Bino-like. This particle couples to ordinary matter chiefly through its interactions with the Higgs sector and the Z boson. The

corresponding effective couplings are given by [2]:¹

$$C_{\tilde{B}\tilde{B}H_{\text{SM}}} = g_1^2 \left(\sin 2\beta + \frac{M_1}{\mu} \right) \frac{v}{\mu}, \quad C_{\tilde{B}\tilde{B}H_{\text{NSM}}} = g_1^2 \cos 2\beta \frac{v}{\mu}, \quad (2.1)$$

$$-iC_{\tilde{B}\tilde{B}A_{\text{NSM}}} = g_1^2 \left(1 + \sin 2\beta \frac{M_1}{\mu} \right) \frac{v}{\mu}, \quad C_{\tilde{B}\tilde{B}Z} = \frac{g_1^3 \cos 2\beta}{2 \sin \theta_W} \frac{v^2}{\mu^2}, \quad (2.2)$$

where $v = 174$ GeV is the electroweak vacuum expectation value (vev), $|M_1|$ represents the DM mass, $H_{\text{SM}} \equiv \sin \beta \text{Re}(H_u^0) + \cos \beta \text{Re}(H_d^0)$ corresponds to the SM Higgs field, and $H_{\text{NSM}} \equiv \cos \beta \text{Re}(H_u^0) - \sin \beta \text{Re}(H_d^0)$ and $A_{\text{NSM}} \equiv \cos \beta \text{Im}(H_u^0) + \sin \beta \text{Im}(H_d^0)$ represent the additional doublet neutral Higgs fields. These interactions give rise to both SI and SD scattering off nucleons. The corresponding cross-sections can be approximated by [3, 20, 21]:

$$\begin{aligned} \sigma_{\tilde{\chi}_1^0, N}^{\text{SI}} &\simeq 2 \times 10^{-48} \text{cm}^2 \times \left(\frac{F_u^N + F_d^N}{0.28} \right)^2 \times \left\{ \frac{F_u^N}{F_u^N + F_d^N} \right. \\ &\quad \times \left[\frac{\cos \alpha}{\sin \beta} \left(\frac{C_{\tilde{\chi}_1^0 \tilde{\chi}_1^0 h}}{0.002} \right) \left(\frac{125 \text{ GeV}}{m_h} \right)^2 + \frac{\sin \alpha}{\sin \beta} \left(\frac{C_{\tilde{\chi}_1^0 \tilde{\chi}_1^0 H}}{0.002} \right) \left(\frac{125 \text{ GeV}}{m_H} \right)^2 \right] + \frac{F_d^N}{F_u^N + F_d^N} \\ &\quad \times \left. \left[-\frac{\sin \alpha}{\cos \beta} \left(\frac{C_{\tilde{\chi}_1^0 \tilde{\chi}_1^0 h}}{0.002} \right) \left(\frac{125 \text{ GeV}}{m_h} \right)^2 + \frac{\cos \alpha}{\cos \beta} \left(\frac{C_{\tilde{\chi}_1^0 \tilde{\chi}_1^0 H}}{0.002} \right) \left(\frac{125 \text{ GeV}}{m_H} \right)^2 \right] \right\}^2, \\ &\simeq 2 \times 10^{-48} \text{cm}^2 \times \\ &\quad \left[\left(\frac{C_{\tilde{B}\tilde{B}H_{\text{SM}}}}{0.002} \right) \left(\frac{125 \text{ GeV}}{m_h} \right)^2 - \cot 2\beta \left(\frac{C_{\tilde{B}\tilde{B}H_{\text{NSM}}}}{0.002} \right) \left(\frac{125 \text{ GeV}}{m_H} \right)^2 \right]^2, \end{aligned} \quad (2.3)$$

$$\sigma_{\tilde{\chi}_1^0, N}^{\text{SD}} \simeq C_N \times \left(\frac{C_{\tilde{\chi}_1^0 \tilde{\chi}_1^0 Z}}{0.1} \right)^2. \quad (2.4)$$

In these expressions, h corresponds to the scalar discovered at the LHC, H denotes heavy doublet-dominated Higgs boson, and F_u^N and F_d^N represent the normalized contributions of up- and down-type quarks to the nucleon mass, respectively. The terms $C_{\tilde{\chi}_1^0 \tilde{\chi}_1^0 h}$, $C_{\tilde{\chi}_1^0 \tilde{\chi}_1^0 H}$, and $C_{\tilde{\chi}_1^0 \tilde{\chi}_1^0 Z}$ quantify the DM couplings to the Higgs bosons h and H , and the Z -boson, respectively. The coefficient C_N relates to the nucleon spin, with values of $C_p \simeq 1.8 \times 10^{-40} \text{ cm}^2$ for protons and $C_n \simeq 1.4 \times 10^{-40} \text{ cm}^2$ for neutrons. The angle α represents the mixing angle between the CP-even Higgs fields H_{SM} and H_{NSM} in forming the mass eigenstates h and H , which satisfies the relationship $\alpha \simeq \beta - \pi/2$ in the large m_A limit [22]. This approximation was employed in deriving the final expression for $\sigma_{\tilde{\chi}_1^0, N}^{\text{SI}}$.

¹For mostly Bino-like DM with small Higgsino admixtures, these couplings give (to a good approximation) the same numerical results as Eqs. (2.4)-(2.6) in Ref. [20]. The differences between the two may be understood as originating from corrections due to higher dimensional operators in Ref. [2], associated with the expansion of the denominator $[1 - (M_1/\mu)^2]$ in powers of M_1^2/μ^2 .

The formulations presented above reveal important suppression mechanisms for DM-nucleon interactions. Specifically, as the Higgsino mass parameter μ increases, the Bino-Higgs coupling becomes suppressed by a factor of $1/\mu$, while the Bino- Z coupling experiences an even stronger suppression by a factor of $1/\mu^2$. As a direct consequence, the SI scattering cross-section $\sigma_{\tilde{\chi}_1^0, N}^{\text{SI}}$ is suppressed by $1/\mu^2$, while the SD scattering cross-section $\sigma_{\tilde{\chi}_1^0, N}^{\text{SD}}$ undergoes a more dramatic reduction by a factor of $1/\mu^4$. In addition, a remarkable cancellation effect occurs when $\sin 2\beta = -M_1/\mu$, causing $C_{\tilde{B}\tilde{B}H_{\text{SM}}} = 0$ to vanish completely. This cancellation leads to a substantial suppression of the SI cross-section $\sigma_{\tilde{\chi}_1^0, N}^{\text{SI}}$ [21].

Before analyzing DM properties in detail, key experimental constraints on the MSSM parameter space can be summarized as follows:

- To naturally accommodate the SM-like Higgs boson mass of approximately 125 GeV, the theory requires $\tan \beta \gtrsim 4$ [23].
- LHC searches for additional Higgs bosons indicate that if the heavy CP-even Higgs boson (H) decays exclusively into SM particles, its mass must exceed 350 GeV, regardless of $\tan \beta$ values [24].
- Compressed spectrum scenarios, where DM coannihilates with electroweakinos to achieve the observed relic abundance, are constrained by LHC experiments. These constraints establish lower mass bounds of approximately 180 GeV for Higgsinos and 220 GeV for Winos [25].
- LHC searches for electroweakinos via multi-lepton and fully hadronic final states set stringent limits within simplified model frameworks: Higgsino mass limits reach ~ 900 GeV for massless DM, while Wino limits extend to 1200 GeV [25, 26]. These limits increase further when light sleptons are present in the decay chain [27].

Light DM scenarios in the MSSM exhibit the following salient features after integrating theoretical formulations with the experimental results:

- The branching ratio for H decaying into DM pairs is significantly suppressed for large μ values. Neglecting this small channel, m_H should exceed 350 GeV. In this regime, the correct relic density can only be obtained through Z - or h -funnel annihilation, requiring $|M_1| \simeq m_Z/2$ or $|M_1| \simeq m_h/2$ [20].
- LZ 2024 constraints on $\sigma_{\tilde{\chi}_1^0, N}^{\text{SD}}$ indicate that for $\tan \beta \gtrsim 4$, the μ parameter must exceed 700 GeV, as demonstrated by Eq. (2.4). Furthermore, analyzing SI cross-section constraints with corresponding formula yields more nuanced boundaries that are dependent on the sign of M_1/μ . Specifically, when $m_A = 1$ TeV, μ must exceed 900 GeV in scenarios where M_1/μ is negative and $\tan \beta \lesssim$

9, or where M_1/μ is positive and $\tan\beta \lesssim 25$. These $\tan\beta$ thresholds increase modestly to 10 and 27, respectively, when $m_A = 2$ TeV. Notably, these direct-detection bounds on μ are independent of Higgsino decay modes and therefore complement the LHC limits.

- The Monte-Carlo simulations presented in this work suggest that for DM annihilation via Z or Higgs resonance, LHC electroweakino searches require $\mu \gtrsim 900$ GeV when Higgsino decay into H is kinematically forbidden.

Based on the preceding analysis, the MSSM encounters significant fine-tuning challenges when accommodating the light DM scenario:

- According to the Z -boson mass expression [28]:

$$m_Z^2 = \frac{2(m_{H_d}^2 + \Sigma_d) - 2(m_{H_u}^2 + \Sigma_u) \tan^2\beta}{\tan^2\beta - 1} - 2\mu^2, \quad (2.5)$$

approximately $m_Z^2/(2\mu^2) \simeq 0.8\%$ parameter fine-tuning is required to predict the correct Z boson mass given that $\mu \gtrsim 700$ GeV [29].

- Since large μ values severely suppress DM couplings to Z and Higgs bosons, achieving the correct cosmic abundance requires the DM mass to approach resonance conditions ($m_Z/2$ or $m_h/2$) with extreme precision, introducing another significant fine-tuning issue [30].

It is worth emphasizing that both instances of fine-tuning arise from a single theoretical demand: the μ -parameter must be comparatively large. This large value, in turn, heavily suppresses all DM couplings.

2.2 Z_3 -NMSSM

In the Z_3 -NMSSM, DM with a mass of several tens of GeV can either be a Bino-dominated lightest neutralino or a Singlino-dominated lightest neutralino. In addition to the couplings shown in Eq. (2.2), the interactions listed below also influence DM phenomenology [2]:

$$\begin{aligned} C_{\tilde{B}\tilde{B}\text{Re}[S]} &= iC_{\tilde{B}\tilde{B}\text{Im}[S]} = -\frac{\lambda g_1^2 \sin 2\beta}{2} \frac{v^2}{\mu_{\text{eff}}^2}, \\ C_{\tilde{B}\tilde{S}H_{\text{SM}}} &= -2\sqrt{2}\lambda g_1 \cos 2\beta \frac{v}{\mu_{\text{eff}}}, \quad iC_{\tilde{B}\tilde{S}A_{\text{NSM}}} = -\sqrt{2}\lambda g_1 \cos 2\beta \frac{(M_1 + M_{\tilde{S}}) v}{\mu_{\text{eff}}^2}, \\ C_{\tilde{B}\tilde{S}H_{\text{NSM}}} &= \sqrt{2}\lambda g_1 \left[2 \sin 2\beta + \frac{(M_1 - M_{\tilde{S}})}{\mu_{\text{eff}}} \right] \frac{v}{\mu_{\text{eff}}}, \\ C_{\tilde{B}\tilde{S}\text{Re}[S]} &= iC_{\tilde{B}\tilde{S}\text{Im}[S]} = \sqrt{2}\lambda^2 g_1 \cos 2\beta \frac{v^2}{\mu_{\text{eff}}^2}, \quad C_{\tilde{B}\tilde{S}Z} = \frac{\sqrt{2}\lambda g_1^2 \sin 2\beta}{\sin \theta_W} \frac{v^2}{\mu_{\text{eff}}^2}, \end{aligned}$$

$$\begin{aligned}
C_{\tilde{S}\tilde{S}H_{\text{SM}}} &= -2\lambda^2 \sin 2\beta \frac{v}{\mu_{\text{eff}}} + 2\lambda^2 \frac{m_{\tilde{S}}v}{\mu_{\text{eff}}^2}, & C_{\tilde{S}\tilde{S}H_{\text{NSM}}} &= -2\lambda^2 \cos 2\beta \frac{v}{\mu_{\text{eff}}}, \\
C_{\tilde{S}\tilde{S}\text{Re}[S]} &= iC_{\tilde{S}\tilde{S}\text{Im}[S]} = \lambda^3 \sin 2\beta \frac{v^2}{\mu_{\text{eff}}^2} - 2\kappa \left(1 - \lambda^2 \frac{v^2}{\mu_{\text{eff}}^2} \right), \\
iC_{\tilde{S}\tilde{S}A_{\text{NSM}}} &= 2\lambda^2 \left[1 - \sin 2\beta \frac{m_{\tilde{S}}}{\mu_{\text{eff}}} \right] \frac{v}{\mu_{\text{eff}}}, & C_{\tilde{S}\tilde{S}Z} &= -\frac{\lambda^2 g_1 \cos 2\beta}{\sin \theta_W} \frac{v^2}{\mu_{\text{eff}}^2},
\end{aligned} \tag{2.6}$$

where $\mu_{\text{eff}} \equiv \lambda \langle S \rangle$ is the effective Higgsino mass, and $M_{\tilde{S}} \equiv 2\kappa\mu_{\text{eff}}/\lambda$ is the Singlino mass. Unlike the interactions in Eq. (2.2), these couplings depend not only on the parameter μ_{eff} but also critically on the Higgs field Yukawa coupling coefficients (λ and κ). When analyzing their impact on DM phenomenology, three fundamental constraints must be considered, as described below:

- Higgs Data Fitting

In the NMSSM, the singlet CP-even Higgs field mixes with the SM Higgs field to form mass eigenstates, consequently modifying the properties of the SM-like Higgs particle. This effect becomes particularly evident when diagonalizing the CP-even Higgs mass matrix. Specially, in the basis $(H_{\text{NSM}}, H_{\text{SM}}, \text{Re}[S])$, the mass matrix takes the following form [18, 19]:

$$\begin{aligned}
\mathcal{M}_{S,11}^2 &= M_A^2 + (m_Z^2 - \lambda^2 v^2) \sin^2 2\beta, & \mathcal{M}_{S,12}^2 &= -\frac{\sin 4\beta}{2}(m_Z^2 - \lambda^2 v^2), \\
\mathcal{M}_{S,13}^2 &= -\lambda \cos 2\beta \left(\frac{M_A^2 \sin 2\beta}{2\mu_{\text{eff}}} + \frac{\kappa \mu_{\text{eff}}}{\lambda} \right) v, & \mathcal{M}_{S,22}^2 &= m_Z^2 \cos^2 2\beta + \lambda^2 v^2 \sin^2 2\beta, \\
\mathcal{M}_{S,23}^2 &= 2\lambda \left[1 - \left(\frac{M_A \sin 2\beta}{2\mu_{\text{eff}}} \right)^2 - \frac{\kappa}{2\lambda} \sin 2\beta \right] \mu_{\text{eff}} v \equiv 2\lambda \delta \mu_{\text{eff}} v, \\
\mathcal{M}_{S,33}^2 &= \lambda^2 \left(\frac{M_A \sin 2\beta}{2\mu_{\text{eff}}} \right)^2 v^2 + \frac{\kappa}{\lambda} \mu_{\text{eff}} A_\kappa + 4 \left(\frac{\kappa}{\lambda} \right)^2 \mu_{\text{eff}}^2 - \frac{1}{2} \lambda \kappa \sin 2\beta v^2 \equiv m_B^2,
\end{aligned}$$

where the parameter δ functions as a measure of the cancellation between different terms in $\mathcal{M}_{S,23}^2$ [31]. The three CP-even mass eigenstates $h_i = \{h, H, h_s\}$ are then acquired through unitary rotations of the matrix V that diagonalizes \mathcal{M}_S^2 , yielding:

$$h_i = V_{h_i}^{\text{NSM}} H_{\text{NSM}} + V_{h_i}^{\text{SM}} H_{\text{SM}} + V_{h_i}^{\text{S}} \text{Re}[S], \tag{2.7}$$

$$C_{\tilde{\chi}\tilde{\chi}h_i} = V_{h_i}^{\text{NSM}} C_{\tilde{\chi}\tilde{\chi}H_{\text{NSM}}} + V_{h_i}^{\text{SM}} C_{\tilde{\chi}\tilde{\chi}H_{\text{SM}}} + V_{h_i}^{\text{S}} C_{\tilde{\chi}\tilde{\chi}\text{Re}[S]}, \quad \tilde{\chi} = \tilde{B}, \tilde{S}. \tag{2.8}$$

Two scenarios can then be further distinguished based on the mass ordering of these CP-even states: the h_1 scenario with $m_h < m_{h_s} < m_H$, and the h_2 scenario with $m_{h_s} < m_h < m_H$. The following approximations are valid in cases with a very massive H [2]:

$$\frac{V_h^{\text{S}}}{V_h^{\text{SM}}} \simeq \frac{\mathcal{M}_{S,23}^2}{(m_h^2 - \mathcal{M}_{S,33}^2)}, \quad V_h^{\text{NSM}} \sim 0, \quad V_h^{\text{SM}} \simeq \sqrt{1 - \left(\frac{V_h^{\text{S}}}{V_h^{\text{SM}}} \right)^2} \sim 1. \tag{2.9}$$

The latest HiggsTools package [32], used to conduct a comprehensive global fit of Higgs properties, then determined that LHC Higgs data constrains $|\mathcal{M}_{S,23}^2/(m_h^2 - \mathcal{M}_{S,33}^2)| \lesssim 0.4$ [33], or equivalently $\lambda\delta\mu_{\text{tot}} \lesssim |\mathcal{M}_{S,33}^2 - m_h^2|/(900 \text{ GeV})$. Quantitatively, $\lambda \lesssim 0.009$ (0.039) when $\mathcal{M}_{S,33} = 100 \text{ GeV}$ (200 GeV), $\mu_{\text{eff}} = 700 \text{ GeV}$, and $\delta \simeq 1$. Furthermore, maintaining perturbativity of the theory up to the GUT scale imposes the additional requirement that $\lambda \lesssim 0.7$ [18].

- Singlino Mass Constraint

Assuming that the Singlino plays a significant role in DM physics, its mass given by $m_{\tilde{s}} = 2\kappa/\lambda\mu_{\text{eff}}$ should be around several tens of GeV. This relationship implies:

$$\kappa \lesssim \frac{\lambda}{20} \times \frac{m_{\tilde{s}}}{100 \text{ GeV}} \times \frac{1 \text{ TeV}}{\mu_{\text{eff}}}. \quad (2.10)$$

Consequently, in light DM scenarios, the parameter κ must be at least one order of magnitude smaller than λ .

- DM-nucleon Scattering

In the NMSSM framework, the SI cross-section for DM-nucleon scattering can be approximated by [2]:

$$\begin{aligned} \sigma_{\tilde{\chi},N}^{\text{SI}} \simeq & 2 \times 10^{-48} \text{ cm}^2 \times \left[\left(\frac{125 \text{ GeV}}{m_h} \right)^2 \left(\frac{C_{\tilde{\chi}\tilde{\chi}h}}{0.002} \right) \right. \\ & \left. + \left(\frac{125 \text{ GeV}}{m_H} \right)^2 \left(\frac{C_{\tilde{\chi}\tilde{\chi}H}}{0.002} \right) + \left(\frac{125 \text{ GeV}}{m_{h_s}} \right)^2 \left(\frac{C_{\tilde{\chi}\tilde{\chi}h_s}}{0.002} \right) \right]^2, \end{aligned} \quad (2.11)$$

where the three terms correspond to exchanges of the SM-like Higgs h , the heavier doublet-like Higgs H , and the singlet-like Higgs h_s , respectively. Meanwhile, the SD cross-section maintains the same form as previously expressed in Eq. (2.2). In the specific case of a Singlino-like DM, more detailed expressions have been thoroughly derived for both cross-sections in Refs. [34–36]. These derivations reveal important relationships, with the primary contribution to the SI cross-section scaling as $\sigma_{\tilde{\chi},N}^{\text{SI}} \propto \lambda^4 v^2 / \mu_{\text{eff}}^2$ for a sufficiently massive h_s or $\propto \lambda^2 \kappa^2$ for a moderately light h_s , while the SD cross-section follows $\sigma_{\tilde{\chi},N}^{\text{SD}} \propto \lambda^4 v^4 / \mu_{\text{eff}}^4$, highlighting the strong dependence of both cross-sections on the λ parameter. LZ 2024 placed significant limitations on this parameter, restricting λ to values as low as approximately 0.01 [36]. This constraint has profound implications for the viability of Singlino-like DM candidates within the NMSSM framework.

When DM is predominantly Bino-like, LZ 2024-based constraints on the SD cross-section require $\mu_{\text{eff}} \gtrsim 700 \text{ GeV}$ for $\tan \beta \gtrsim 4$, as in the MSSM. In addition to

the canonical Z and h resonant annihilation channels, DM may also co-annihilate with Singlino when the Bino and Singlino masses are nearly degenerate [2], or proceed through h_s and A_s resonant channels to achieve the experimentally measured relic abundance [30, 37, 38]. The relevant interactions — including $C_{\tilde{B}\tilde{B}\text{Re}[S]}$, $C_{\tilde{B}\tilde{B}\text{Im}[S]}$, $C_{\tilde{B}\tilde{S}H_{\text{SM}}}$, $C_{\tilde{B}\tilde{S}\text{Re}[S]}$, $C_{\tilde{B}\tilde{S}\text{Im}[S]}$, $C_{\tilde{B}\tilde{S}Z}$, $C_{\tilde{S}\tilde{S}H_{\text{SM}}}$, $C_{\tilde{S}\tilde{S}\text{Re}[S]}$, $C_{\tilde{S}\tilde{S}\text{Im}[S]}$, and $C_{\tilde{S}\tilde{S}Z}$ — are all suppressed by a factor of $1/\mu_{\text{eff}}$ and typically also by λ . This suppression necessitates fine-tuning to reproduce the observed relic density.

For Singlino-dominated DM, LZ 2024 constraints on both SI and SD cross-sections require $\lambda \lesssim 0.05$, although definitive lower bounds cannot be established on μ_{eff} [36]. Complementarily, LHC constraints on compressed spectrum scenarios mandate $\mu_{\text{eff}} \gtrsim 180$ GeV [25], while LHC searches for electroweakinos via multi-lepton channels impose even stronger constraints in other scenarios [25–27]. As a result, all interactions in Eq. (2.6) are significantly suppressed by λ or κ , where $\kappa \lesssim \lambda/4$ according to Eq.(2.10) and the LHC restrictions on μ_{eff} . Under these circumstances, annihilation processes such as $\tilde{S}\tilde{S} \rightarrow h_s A_s, h_s h_s, A_s A_s$ cannot generate the observed relic density due to the extremely small value of κ . Conversely, resonant h_s or A_s annihilation requires substantial fine-tuning, since the coupling strengths $C_{\tilde{S}\tilde{S}\text{Re}[S]}$ and $C_{\tilde{S}\tilde{S}\text{Im}[S]}$ are weak [36].

The takeaway from the above discussion is clear: because every DM coupling is highly suppressed, the Z_3 -NMSSM requires severe fine-tuning to accommodate a viable light DM candidate.

2.3 GNMSSM

In contrast to the Z_3 -NMSSM, the GNMSSM drops the rigid Z_3 symmetry and incorporates all renormalizable operators in the singlet–Higgs sector. Beyond the familiar $\lambda \hat{S} \hat{H}_u \cdot \hat{H}_d$ and $\kappa \hat{S}^3/3$ terms, the superpotential includes an explicit Higgsino mass term $\mu \hat{H}_u \cdot \hat{H}_d$, a singlet Majorana mass term $\mu' \hat{S}^2/2$, and optionally a linear tadpole term $\xi \hat{S}$ [18, 39]. These Z_3 -violating terms simultaneously resolve the cosmological domain-wall problem [39–43] and eliminate dangerous higher-order tadpoles [18, 44], while preserving theoretical motivation through discrete R -symmetries that naturally generate μ and μ' at the weak scale [39–43]. Although the Bino and Singlino interactions in the GNMSSM remain the same as those of the Z_3 -NMSSM, the enlarged superpotential decouples several key mass parameters [36, 45]. Specifically, the Higgsino mass μ_{tot} and the Singlino mass $m_{\tilde{S}}$ can be expressed as:

$$\mu_{\text{tot}} = \lambda \langle S \rangle + \mu, \quad m_{\tilde{S}} = 2\kappa \langle S \rangle + \mu', \quad (2.12)$$

allowing them to be adjusted independently. These formulae represents a critical departure from the Z_3 -NMSSM, in which the Singlino mass differs from the Higgsino mass only by a factor of $2\kappa/\lambda$, where κ must be less than $\lambda/2$ for viable Singlino-like DM scenarios and $\lambda/4$ if the DM is further required to be lighter than 100 GeV. In

contrast, the GNMSSM permits $|\kappa|$ to be much larger than λ in this scenario [35]. This freedom profoundly alters Singlino DM phenomenology while leaving Bino-like DM properties essentially unchanged.

A Singlino-like DM $\tilde{\chi}_1^0$, the lightest supersymmetric particle (LSP) with a mass of $|m_{\tilde{\chi}_1^0}| \simeq |m_{\tilde{S}}|$, can thus annihilate through “secluded sector” channels controlled by κ , e.g., $\tilde{\chi}_1^0 \tilde{\chi}_1^0 \rightarrow h_s A_s, h_s h_s, A_s A_s$. Consequently, the thermally averaged cross-section exhibits a characteristic κ^4 dependence [36]. In contrast, the direct detection cross-section, which is proportional to λ^4 or $\lambda^2 \kappa^2$ like the Z_3 -NMSSM, remains naturally suppressed due to the small value of λ [36]. This separation of roles offers a substantially broader DM parameter space, capable of simultaneously accommodating relic density observations and direct detection bounds, particularly obviating the need for the resonance enhancements in the annihilation [35, 36]. In addition, smaller λ values in viable regions enhance quartic self-coupling stability, thereby mitigating potential issues with color- or charge-breaking vacua that can plague certain regions of the Z_3 -NMSSM parameter space [46, 47].

From the collider perspective, the LHC phenomenology of GNMSSM may present both challenges and opportunities. For instance, the scalar and neutralino spectrum is enriched, as singlet scalar masses m_{h_s}, m_{A_s} and the Singlino mass $m_{\tilde{S}}$ can be set independently, leading to diverse and potentially distinctive collider signatures [45]. Supersymmetric particle decay chains can be longer and more intricate, with significant momentum transfer to particles in the secluded sector [35]. While this may reduce the sensitivity of conventional searches, with Higgsino masses as low as about 200 GeV, it also opens new avenues for novel detection strategies [48].

In summary, the GNMSSM represents a well-motivated extension of the conventional Z_3 -NMSSM, offering greater theoretical consistency and phenomenological flexibility. By introducing μ , μ' , and optionally ξ terms that break the Z_3 symmetry, this enables λ and κ to play distinct roles in DM physics: λ can remain minimal to satisfy direct detection constraints, while κ can assume larger values to dominate DM self-annihilation processes. This characteristic makes the GNMSSM framework particularly attractive for addressing contemporary challenges in supersymmetry, naturalness, DM phenomenology, and Higgs physics in a coherent and less fine-tuned manner. As demonstrated below, this theory naturally predicts a viable DM candidate with a mass of several tens of GeV, since several key DM couplings remain appreciable even after all experimental constraints have been applied.

3 Comprehensive study of GNMSSM

This section presents a comprehensive numerical framework for studying light DM in the GNMSSM. The model was built using the SARAH-4.15.3 [49–52] package. The particle spectra and flavor observables were calculated by the SPheno-4.0.5 [53],

[54] and FlavorKit [55] codes, respectively. DM observables were computed with micrOMEGAs-5.0.4 [56–61] code.

3.1 Research strategy

A joint likelihood function \mathcal{L} was first formulated to guide the sampling process and accurately delineate the GNMSSM parameter space as follows:

$$\begin{aligned} \mathcal{L} &\equiv \mathcal{L}_{\Omega h^2} \times \mathcal{L}_{\text{LZ}} \times \mathcal{L}_{\text{Const}}, \\ \mathcal{L}_{\Omega h^2} &= \exp \left[-\frac{1}{2} \left(\frac{\Omega h^2 - 0.120}{0.012} \right)^2 \right], \quad \mathcal{L}_{\text{LZ}} = \exp \left(-\frac{\sigma_{\text{eff}}^{\text{SI}}}{2\delta_\sigma^2} \right), \\ \mathcal{L}_{\text{Const}} &= \begin{cases} 1 & \text{if satisfying all experimental constraints} \\ \exp(-100) & \text{otherwise} \end{cases}. \end{aligned} \quad (3.1)$$

In this construction, the relic abundance Ωh^2 is assumed to follow a Gaussian distribution $\mathcal{L}_{\Omega h^2}$, with its central value derived from the Planck experiment [62] and a theoretical uncertainty of 10%. Given the smallness of the SI scattering cross-section and consequently σ_p^{SI} may significantly deviate from σ_n^{SI} , the effective SI cross-section in the Gaussian likelihood term \mathcal{L}_{LZ} is defined as $\sigma_{\text{eff}}^{\text{SI}} = 0.169\sigma_p^{\text{SI}} + 0.347\sigma_n^{\text{SI}} + 0.484\sqrt{\sigma_p^{\text{SI}} \times \sigma_n^{\text{SI}}}$ [63] for comparison with the results from LZ 2022 [64]. The variance square is then given by $\delta_\sigma^2 \equiv \text{UL}_\sigma^2/1.64^2 + (0.2\sigma)^2$, where UL_σ refers to the 90% C. L. upper limit on the SI scattering cross-section, and 0.2σ accounts for uncertainties [65]. The $\mathcal{L}_{\text{Const}}$ term encompasses the following experimental constraints:

- **Higgs data fit:** The properties of h must align with the LHC Higgs data at 95% C.L. This alignment is enforced by the `HiggsSignal 2.6.2` code [66–69] with the requirement that the p -value is greater than 0.05, where a 3 GeV combined theoretical and experimental uncertainty for m_h is also considered. In addition, `HiggsTools-1.2` [32], which incorporates 129 Higgs observables, was used to update constraints from the Higgs data by imposing the condition $\Delta\chi^2 \equiv \chi^2_{\text{Higgs}} - \chi^2_{\text{SM},125} \lesssim 6.18$, where $\chi^2_{\text{SM},125} \simeq 176.3$ corresponds to a pure SM Higgs boson in the GNMSSM [33].
- **Extra Higgs searches:** The `HiggsBounds 5.10.2` code [70–74] was employed to conduct comprehensive searches for additional Higgs bosons beyond the SM at LEP, Tevatron and LHC. This search was further complemented by `HiggsTools-1.2` [32] with enhanced search capabilities.
- **Indirect DM searches:** The Fermi-LAT collaboration has accumulated years of dwarf galaxy observations, yielding constraints on DM annihilation cross-sections². The likelihood function from Refs. [75, 76] was applied to evaluate

²see: www-glast.stanford.edu/pub_data/1048

Table 1. An exploration of the parameter space for the h_1 scenario. All inputs were assumed to exhibit a flat prior distribution, reflecting their physical meaning in the small λ case as shown in Ref. [45]. The parameter v_s was defined as $\sqrt{2}\langle S \rangle$, and m_B and m_C are the mass parameters for the CP-even and -odd singlet Higgs fields, respectively. The soft trilinear coefficients for the third-generation squarks were set equal ($A_t = A_b$) for simplicity and allowed to vary due to their significant radiative corrections to the SM-like Higgs boson mass. We fixed $M_1 = 150$ GeV, $M_3 = 3$ TeV, and set all other unmentioned dimensional parameters to 2 TeV. All parameters were defined at the renormalization scale $Q_{\text{input}} = 1$ TeV. The h_2 scenario shared the same parameter space as in the h_1 scenario, except that $5 \text{ GeV} \leq m_B \leq 130 \text{ GeV}$.

Parameter	Prior	Range	Parameter	Prior	Range
λ	Flat	$10^{-3} - 0.2$	$\mu_{\text{tot}}/\text{GeV}$	Flat	$200 - 1000$
κ	Flat	$-0.7 - 0.7$	m_B/GeV	Flat	$95 - 250$
δ	Flat	$-1.0 - 1.0$	m_C/GeV	Flat	$5 - 250$
$\tan \beta$	Flat	$1 - 60$	$m_{\tilde{S}}/\text{GeV}$	Flat	$-102 - 102$
v_s/GeV	Flat	$1 - 10^3$	A_t/TeV	Flat	$-5.0 - 5.0$

these bounds. The latest MADHAT package [77, 78], which integrates 14 years of public Fermi-LAT data from 54 dwarf spheroidal galaxies, was also employed to enhance the robustness of this analysis.

- **B -physics observables:** The branching ratios of $B_s \rightarrow \mu^+ \mu^-$ and $B \rightarrow X_s \gamma$ should agree with experimental measurements at the 2σ level [79].

Eq. (3.1) was used to implement the MultiNest algorithm with $n_{\text{live}} = 8000$ [94] and conduct comprehensive scans over the parameter space shown in Table 1. Samples obtained in this way was then surveyed to see their compatibility with LHC-based electroweakino search results. This was done by performing a series of Monte Carlo simulations for the following production channels:

$$\begin{aligned} pp \rightarrow \tilde{\chi}_\alpha^0 \tilde{\chi}_\beta^0, \quad \alpha, \beta = 2, 3, 4, 5; \quad \alpha \leq \beta, \\ pp \rightarrow \tilde{\chi}_i^\pm \tilde{\chi}_j^\mp, \quad i, j = 1, 2, \\ pp \rightarrow \tilde{\chi}_\alpha^0 \tilde{\chi}_i^\pm, \quad \alpha = 2, 3, 4, 5; \quad i = 1, 2. \end{aligned} \tag{3.2}$$

In this process, corresponding cross-sections were first calculated to next-to-leading order (NLO) using program Prospino2 [95], with LHC fast simulations conducted by the SModelS-3.0.0 [96] tool. Specifically, we selected all analyses included in the smodels-database-release-3.0.0 and combined signal regions when available, to provide a preliminary assessment. Given the exclusion capabilities of SModelS-3.0.0 are limited by the database and strict working prerequisites, we further examined surviving samples by simulating with the Monte-Carlo method the analyses listed in Table 2. In more detail, we generated 10^5 events for these processes

Table 2. LHC analyses for electroweakino pair production included in this study, categorized by final-state signatures.

Scenario	Final State	Analysis
$\tilde{\chi}_1^+ \tilde{\chi}_1^- \rightarrow 2\tilde{\ell}\nu(\ell\bar{\nu})$	$2\ell + E_T^{\text{miss}}$	ATLAS-CONF-2016-096($13.3 fb^{-1}$) [80] ATLAS-1908-08215($139 fb^{-1}$) [81]
$\tilde{\chi}_1^+ \tilde{\chi}_1^- \rightarrow WW\tilde{\chi}_1^0\tilde{\chi}_1^0$	$2\ell + E_T^{\text{miss}}$	ATLAS-1908-08215($139 fb^{-1}$) [81]
$\tilde{\chi}_2^0\tilde{\chi}_1^\pm \rightarrow \ell\bar{\ell}\tilde{\nu}(\ell\bar{\nu}\nu\bar{\nu})$	$3\ell + E_T^{\text{miss}}$	ATLAS-CONF-2016-096($13.3 fb^{-1}$) [80] ATLAS-1803-02762($36.1 fb^{-1}$) [82] CMS-SUS-16-039($35.9 fb^{-1}$) [83]
$\tilde{\chi}_2^0\tilde{\chi}_1^\pm \rightarrow WZ\tilde{\chi}_1^0\tilde{\chi}_1^0$	$3\ell + E_T^{\text{miss}}$	ATLAS-2106-01676($139 fb^{-1}$) [25] ATLAS-CONF-2019-020($139 fb^{-1}$) [84]
$\tilde{\chi}_1^0\tilde{\chi}_2^0 \rightarrow Z\tilde{\chi}_1^0\tilde{\chi}_1^0$ $\tilde{\chi}_1^0\tilde{\chi}_1^\pm \rightarrow W\tilde{\chi}_1^0\tilde{\chi}_1^0$ $\tilde{\chi}_2^0\tilde{\chi}_1^\pm \rightarrow WZ\tilde{\chi}_1^0\tilde{\chi}_1^0$ $\tilde{\chi}_1^+\tilde{\chi}_1^- \rightarrow WW\tilde{\chi}_1^0\tilde{\chi}_1^0$	$n\ell(n \geq 4) + E_T^{\text{miss}}$	ATLAS-2103-11684($139 fb^{-1}$) [85]
$\tilde{\chi}_2^0\tilde{\chi}_1^\pm \rightarrow \tau\bar{\tau}\tilde{\tau}\nu$	$3\tau + E_T^{\text{miss}}$	CMS-SUS-16-039($35.9 fb^{-1}$) [83]
$\tilde{\chi}_2^0\tilde{\chi}_1^\pm \rightarrow \ell\bar{\ell}\tilde{\tau}\nu$	$2\ell + 1\tau + E_T^{\text{miss}}$	CMS-SUS-16-039($35.9 fb^{-1}$) [83]
$\tilde{\chi}_2^0\tilde{\chi}_1^\pm \rightarrow WZ\tilde{\chi}_1^0\tilde{\chi}_1^0$ $\tilde{\chi}_1^+\tilde{\chi}_1^- \rightarrow WW\tilde{\chi}_1^0\tilde{\chi}_1^0$	$2j(\text{large}) + E_T^{\text{miss}}$	ATLAS-2108-07586($139 fb^{-1}$) [26]
$\tilde{\chi}_2^0\tilde{\chi}_3^0 \rightarrow ZZ(Zh)\tilde{\chi}_1^0\tilde{\chi}_1^0$ $\tilde{\chi}_2^0\tilde{\chi}_1^\pm \rightarrow WZ(Wh)\tilde{\chi}_1^0\tilde{\chi}_1^0$	$j(\text{large}) + b(\text{large}) + E_T^{\text{miss}}$	ATLAS-2108-07586($139 fb^{-1}$) [26]
$\tilde{\chi}_2^0\tilde{\chi}_1^\pm \rightarrow WZ\tilde{\chi}_1^0\tilde{\chi}_1^0$	$2\ell(\text{soft}) + jets + E_T^{\text{miss}}$	CMS-PAS-SUS-16-025($12.9 fb^{-1}$) [86]
$\tilde{\chi}_2^0\tilde{\chi}_1^\pm \rightarrow WZ\tilde{\chi}_1^0\tilde{\chi}_1^0$	$n\ell(n \geq 2) + nj(n \geq 0) + E_T^{\text{miss}}$	ATLAS-1712-08119($36.1 fb^{-1}$) [87] ATLAS-1803-02762($36.1 fb^{-1}$) [82] ATLAS-1911-12606($139 fb^{-1}$) [88] ATLAS-2106-01676($139 fb^{-1}$) [25] CMS-SUS-16-039($35.9 fb^{-1}$) [83] CMS-SUS-16-048($35.9 fb^{-1}$) [89] CMS-SUS-20-001($137 fb^{-1}$) [90]
$\tilde{\chi}_1^0\tilde{\chi}_1^0 \rightarrow ZZ(Zh)(hh)\tilde{G}\tilde{G}$	$n\ell(n \geq 2) + nj(n \geq 0) + E_T^{\text{miss}}$	CMS-SUS-16-039($35.9 fb^{-1}$) [83] CMS-SUS-20-001($137 fb^{-1}$) [90]
$\tilde{\chi}_2^0\tilde{\chi}_1^\pm \rightarrow Wh\tilde{\chi}_1^0\tilde{\chi}_1^0$	$n\ell(n \geq 1) + nb(n \geq 0) + nj(n \geq 0) + E_T^{\text{miss}}$	ATLAS-1909-09226($139 fb^{-1}$) [91] CMS-SUS-16-039($35.9 fb^{-1}$) [83]
$\tilde{\chi}_2^0\tilde{\chi}_1^\pm \rightarrow Wh\tilde{\chi}_1^0\tilde{\chi}_1^0$	$2\gamma + nl(n \geq 1) + E_T^{\text{miss}}$	ATLAS-2004-10894($139 fb^{-1}$) [92]
$\tilde{\chi}_2^0\tilde{\chi}_1^\pm \rightarrow Wh\tilde{\chi}_1^0\tilde{\chi}_1^0$	$2\gamma + nj(n \geq 2) + E_T^{\text{miss}}$	ATLAS-2004-10894($139 fb^{-1}$) [92]
$\tilde{\chi}_2^0\tilde{\chi}_1^\mp \rightarrow Wh(WZ)\tilde{\chi}_1^0\tilde{\chi}_1^0$ $\tilde{\chi}_1^+\tilde{\chi}_1^- \rightarrow WW\tilde{\chi}_1^0\tilde{\chi}_1^0$	$2\gamma + n\ell(n \geq 0) + nb(n \geq 0) + nj(n \geq 0) + E_T^{\text{miss}}$	ATLAS-1802-03158($36.1 fb^{-1}$) [93]

using program `MadGraph_aMC@NLO` [97, 98], and implemented parton showers and hadronization using `PYTHIA8` [99]. The resulting event files were then fed into the `CheckMATE-2.0.37` [100–102] package, which integrates the modular `DELPHES-3.5` [103]

Table 3. Primary annihilation channels and their proportions for light DM in both h_1 and h_2 scenarios, with $M_1 = 150$ GeV and $f = u, d, c, s, b, \tau$. The first row of each scenario takes into account all samples that meet LZ 2024 constraints. The second row corresponds to those further satisfying the LHC constraints, namely predicting an R value less than unity.

Scenario	Sample Size	$\tilde{\chi}_1^0 \tilde{\chi}_1^0 \rightarrow h_s h_s$	$\tilde{\chi}_1^0 \tilde{\chi}_1^0 \rightarrow A_s A_s$	$\tilde{\chi}_1^0 \tilde{\chi}_1^0 \rightarrow h_s A_s$	$\tilde{\chi}_1^0 \tilde{\chi}_1^0 \rightarrow f \bar{f}$
h_1	8983	0	98.3%	1.0%	0.6%
	6379	0	98.3%	1.2%	0.4%
h_2	6155	0	9.8%	90.0%	0
	4874	0	9.1%	90.8%	0

framework for detector simulations. The R value, defined as $R \equiv \max\{S_i/S_{i,obs}^{95}\}$, was subsequently calculated for all involved analyses, where S_i represents a simulated event number for the i -th signal region (SR) and $S_{i,obs}^{95}$ is the corresponding 95% C.L. upper limit. A value of $R > 1$ typically implies the sample is experimentally excluded if the involved uncertainties are neglected [104], while $R < 1$ indicates consistency with experimental data.

3.2 Numerical results

The included parameter space scan produced 23732 samples for the h_1 scenario and 21724 samples for the h_2 scenario. It is notable that the LZ experiment recently published its 2024 results [4], prompting us to refine these samples using new constraints that significantly reduced sample sizes to 8983 and 6155, respectively. The previously mentioned LHC constraints further narrowed the surviving samples to 6379 for the h_1 scenario and 4874 for the h_2 scenario.

To characterize light DM properties comprehensively, Table 3 classifies samples satisfying both the LZ 2024 constraints and the LHC threshold criteria $R < 1$ by their dominant annihilation channels. The analysis identifies $\tilde{\chi}_1^0 \tilde{\chi}_1^0 \rightarrow A_s A_s$ as the predominant channel in the h_1 scenario. This p -wave process proceeds under the threshold conditions $|m_{\tilde{\chi}_1^0}| \gtrsim m_{A_s}$ and $m_{h_s} \gtrsim 2|m_{\tilde{\chi}_1^0}| - m_{A_s}$. At freeze-out temperature, the thermally-averaged cross-section $\langle \sigma v \rangle_{x_F}^{A_s A_s}$ can be approximated by [10]:

$$\begin{aligned} \langle \sigma v \rangle_{x_F}^{A_s A_s} &\simeq \frac{v_F^2}{128\pi m_{\tilde{\chi}_1^0}^2} \sqrt{1 - \frac{m_{A_s}^2}{m_{\tilde{\chi}_1^0}^2}} \\ &\times 8\kappa^4 \left\{ \frac{1}{3} \frac{[(\frac{m_{A_s}}{m_{\tilde{\chi}_1^0}})^2 - 1]^2}{[\frac{1}{2}(\frac{m_{A_s}}{m_{\tilde{\chi}_1^0}})^2 - 1]^4} + \frac{(\frac{A_\kappa - m_{\tilde{S}}}{m_{\tilde{\chi}_1^0}})^2}{[(\frac{m_{h_s}}{m_{\tilde{\chi}_1^0}})^2 - 4]^2 + (\frac{m_{h_s}}{m_{\tilde{\chi}_1^0}})^2 (\frac{\Gamma_{h_s}}{m_{\tilde{\chi}_1^0}})^2} \right\}, \end{aligned} \quad (3.3)$$

where $v_F \simeq 0.3$ represents the DM velocity at freeze-out. The first and second terms in the braces arise from t - and s -channel Feynman diagrams, respectively. This formula reveals several key features:

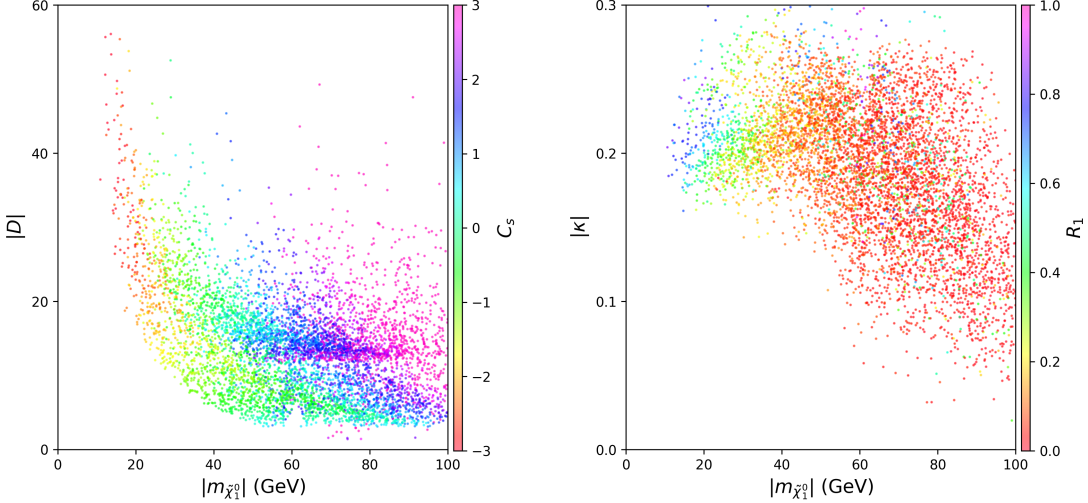


Figure 1. Scatter plots for samples dominated by $\tilde{\chi}_1^0 \tilde{\chi}_1^0 \rightarrow A_s A_s$ annihilation and satisfying all experimental constraints in the h_1 scenario. Left panel: $|D| \equiv |(A_\kappa - m_{\tilde{S}})/m_{\tilde{\chi}_1^0}|$ versus $|m_{\tilde{\chi}_1^0}|$, with color scale C_s defined by $2\{\ln |(A_\kappa - m_{\tilde{S}})/m_{\tilde{\chi}_1^0}| - \ln |(m_{h_s}/m_{\tilde{\chi}_1^0})^2 - 4|\}\}$, indicating relative s -channel strength in Eq. (3.3). Right panel: $|\kappa|$ versus $|m_{\tilde{\chi}_1^0}|$, colored by the squared mass ratio $R_1 \equiv (m_{A_s}/m_{\tilde{\chi}_1^0})^2$.

- **Non-interference property:** The s - and t -channel contributions do not interfere. Both scale as $\kappa^4/m_{\tilde{\chi}_1^0}^2$, modulated by a common phase-space factor $\sqrt{1 - R_1}$ with $R_1 \equiv (m_{A_s}/m_{\tilde{\chi}_1^0})^2$.
- **t -channel behavior:** For fixed $m_{\tilde{\chi}_1^0}$, the t -channel contribution depends solely on κ and the squared mass ratio R_1 . When normalized to its value at $R_1 = 0$, it equals approximately 0.87, 0.68, 0.42, and 0.14 for $R_1 = 0.2, 0.4, 0.6$, and 0.8, respectively — decreasing monotonically as R_1 grows. Thus, its overall contribution is more sensitive to κ than to the squared mass ratio R_1 .
- **s -channel complexity:** In contrast to the t -channel, the s -channel contribution depends on additional parameters: the mass of h_s , its width Γ_{h_s} , and the combination $D \equiv (A_\kappa - m_{\tilde{S}})/m_{\tilde{\chi}_1^0}$ arising from the $h_s A_s A_s$ coupling. Among the samples from our scan, Γ_{h_s} remains very small and h_s rarely approaches resonance during annihilation. Consequently, the width term can be safely neglected.
- **Magnitude comparison:** While the t -channel amplitude in braces never exceeds $1/3$, the s -channel component can reach several orders of magnitude larger when $|D|$ is substantial and m_{h_s} approaches $2|m_{\tilde{\chi}_1^0}|$. Consequently, the s -channel annihilation often governs the relic density.

Figure 1 projects the samples dominated by $\tilde{\chi}_1^0 \tilde{\chi}_1^0 \rightarrow A_s A_s$ annihilation onto the $|m_{\tilde{\chi}_1^0}| - |D|$ and $|m_{\tilde{\chi}_1^0}| - |\kappa|$ planes. Compared to the full parameter space defined

in Table 1, accommodating the observed relic density while satisfying the LZ 2024 constraints requires $|\kappa| \lesssim 0.3$ and $|m_{\tilde{\chi}_1^0}| \gtrsim 10$ GeV. Further analysis reveals distinct mass-dependent behaviors across three regimes:

- **Light DM regime (10 – 30 GeV):** As shown in the left panel of Fig. 1, the s -channel contribution remains subdominant due to $m_{h_s}^2 \gg m_{\tilde{\chi}_1^0}^2$, given that m_{h_s} exceeds 125 GeV. It gradually strengthens and becomes comparable with the t -channel as $|m_{\tilde{\chi}_1^0}|$ approaches 30 GeV. By contrast, despite substantial R_1 values (numerically $0.6 \lesssim R_1 \lesssim 0.8$) that suppress the t -channel amplitude, sufficiently large κ ensures t -channel dominance in determining the relic abundance, as illustrated in the right panel of Fig. 1.
- **Intermediate masses (30 – 60 GeV):** The s -channel contribution increases progressively and begins to surpass the t -channel, which diminishes due to its inverse proportionality to $m_{\tilde{\chi}_1^0}^2$.
- **Heavy DM regime (> 60 GeV):** A dramatic transition occurs wherein the s -channel typically dominates and intensifies further with increasing mass. This dominance arises through two mechanisms. First, most samples satisfy $0.6 \lesssim m_{h_s}/(2|m_{\tilde{\chi}_1^0}|) \lesssim 1.4$, where near-resonance effects enhance the s -channel. Second, for samples far from resonance, $|A_\kappa/m_{\tilde{\chi}_1^0}|$ becomes sufficiently large to ensure s -channel dominance. These mechanisms allow κ as low as 0.04 to produce the measured abundance at $|m_{\tilde{\chi}_1^0}| \simeq 100$ GeV.

In the h_2 scenario, DM achieves the observed relic abundance primarily through the s -wave annihilation channel $\tilde{\chi}_1^0 \tilde{\chi}_1^0 \rightarrow h_s A_s$, as listed in Table 3. This process requires the kinematic condition $2|m_{\tilde{\chi}_1^0}| \gtrsim m_{h_s} + m_{A_s}$, suggesting that all the singlet-dominated particles are likely to be simultaneously light. Compared with the h_1 scenario with a massive h_s , the h_2 case is more tightly constrained by current Higgs coupling measurements and by LHC searches for exotic decays of the SM-like Higgs boson [105]. The underlying reason is that, according to the approximation in Eq. (2.9), h typically contains a more substantial singlet admixture in this scenario. Consequently, its couplings to singlet-dominated states become stronger when κ is sizable, leading to potentially large branching fractions for exotic decays such as $h \rightarrow \tilde{\chi}_1^0 \tilde{\chi}_1^0, h_s h_s$, and $A_s A_s$.

The combined constraints from Higgs physics and the measured relic density yield a preferred particle spectrum characterized by $m_{h_s} > |m_{\tilde{\chi}_1^0}| \gtrsim 60$ GeV and $m_{A_s}^2/m_{\tilde{\chi}_1^0}^2 < 1/4$ for most samples, with an absolute upper limit of $m_{A_s}^2/m_{\tilde{\chi}_1^0}^2 < 1/2$ across all surviving samples. These features are illustrated in the left panel of Fig. 2, where samples dominated by the $\tilde{\chi}_1^0 \tilde{\chi}_1^0 \rightarrow h_s A_s$ annihilation channel are projected onto $R_2 \equiv m_{h_s}^2/m_{\tilde{\chi}_1^0}^2$ versus $|m_{\tilde{\chi}_1^0}|$ plane. The color scale $C_t \equiv 8m_{A_s}^2/(4m_{\tilde{\chi}_1^0}^2 - m_{h_s}^2)$ quantifies the partial t -channel contribution as introduced below. The right panel

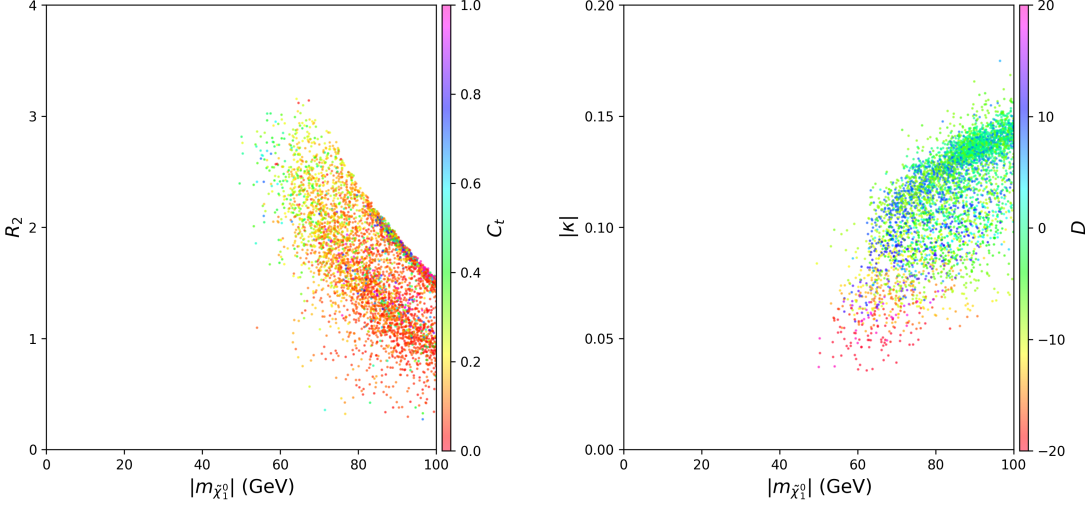


Figure 2. Scatter plots for samples dominated by $\tilde{\chi}_1^0 \tilde{\chi}_1^0 \rightarrow h_s A_s$ annihilation and satisfying all experimental constraints in the h_2 scenario. Left panel: $R_2 \equiv (m_{h_s}/m_{\tilde{\chi}_1^0})^2$ versus $|m_{\tilde{\chi}_1^0}|$, with a color bar C_t defined by $8m_{A_s}^2/(4m_{\tilde{\chi}_1^0}^2 - m_{h_s}^2)$, which measures the partial t -channel contributions of Eq. (3.4). Right panel: $|\kappa|$ versus $|m_{\tilde{\chi}_1^0}|$, with a color bar representing the s -channel contribution $D \equiv (A_\kappa - m_{\tilde{S}})/m_{\tilde{\chi}_1^0}$ in Eq. (3.4).

displays the same samples in $|\kappa|$ versus $|m_{\tilde{\chi}_1^0}|$ plane, where the color variable $D \equiv (A_\kappa - m_{\tilde{S}})/m_{\tilde{\chi}_1^0}$ represents the combination governing the s -channel contribution.

The thermally-averaged cross-section at freeze-out for this channel, $\langle \sigma v \rangle_{x_F}^{h_s A_s}$, is expressed as [2, 36, 106]:

$$\langle \sigma v \rangle_{x_F}^{h_s A_s} \simeq \frac{1}{256\pi m_{\tilde{\chi}_1^0}^2} \left\{ \left[4 - \frac{(m_{h_s} + m_{A_s})^2}{m_{\tilde{\chi}_1^0}^2} \right] \left[4 - \frac{(m_{h_s} - m_{A_s})^2}{m_{\tilde{\chi}_1^0}^2} \right] \right\}^{1/2} |\mathcal{A}_s + \mathcal{A}_t|^2,$$

where the s - and t -channel amplitudes, \mathcal{A}_s and \mathcal{A}_t , depends primarily on the spectrum and couplings of the singlet-dominated fields. For small λ and $m_{A_s}^2 \ll 4m_{\tilde{\chi}_1^0}^2$, this expression simplifies to:

$$\langle \sigma v \rangle_{x_F}^{h_s A_s} \simeq \frac{1}{256\pi m_{\tilde{\chi}_1^0}^2} \left[4 - \left(\frac{m_{h_s}}{m_{\tilde{\chi}_1^0}} \right)^2 \right] |\mathcal{A}_s + \mathcal{A}_t|^2, \quad (3.4)$$

with the amplitudes approximated as:

$$\mathcal{A}_s \simeq \kappa^2 D, \quad \mathcal{A}_t \simeq \kappa^2 (4 + C_t). \quad (3.5)$$

The color coding in Fig. 2 reveals that the amplitude \mathcal{A}_s varies substantially from $-20\kappa^2$ to $20\kappa^2$, while \mathcal{A}_t remains relatively stable between $4\kappa^2$ to $5\kappa^2$. The sign of \mathcal{A}_s determines whether it interferes constructively or destructively with \mathcal{A}_t , thereby significantly affecting the required magnitude of κ for achieving the measured relic density. Specifically, when $D \simeq 20$, the s -channel contribution dominates and constructive interference allows $|\kappa|$ as low as 0.03 for $|m_{\tilde{\chi}_1^0}| \simeq 100$ GeV to acquire the

density. Conversely, in the $|D| \lesssim 10$ regime — which characterizes the majority of surviving samples — the two amplitudes become comparable. When destructive interference occurs, larger $|\kappa|$ values up to 0.16 are necessary at $|m_{\tilde{\chi}_1^0}| \simeq 100$ GeV to compensate for the reduced total amplitude. These relationships are evident in the right panel of Fig. 2.

We clarify that in the h_2 scenario, the singlet-like Higgs mass satisfies $m_{h_s} \lesssim 125$ GeV and this upper limit is consistently achieved when $|m_{\tilde{\chi}_1^0}| \gtrsim 70$ GeV for the obtained samples. Consequently, the maximum reach of R_2 decreases monotonically with increasing $|m_{\tilde{\chi}_1^0}|$, as seen in the left panel of Fig. 2. Besides, since $\langle \sigma v \rangle_{x_F}^{h_s A_s}$ is proportional to $\kappa^4/m_{\tilde{\chi}_1^0}^2$, larger $|\kappa|$ values are required to maintain the measured relic abundance as $|m_{\tilde{\chi}_1^0}|$ increases, a trend clearly visible in the right panel. Additionally, as exhibited by the correlation between the two panels, for fixed $|m_{\tilde{\chi}_1^0}| \simeq 60$ GeV, an increase in R_2 — arising from enhanced m_{h_s} and consequently reduced annihilation phase space — requires a correspondingly larger $\kappa^2 D$ to preserve the measured relic density. This reflects the interplay of the parameters.

Next, we turn to DM–nucleon scattering. For $m_{h_s} \lesssim 250$ GeV and $m_H \simeq 2$ TeV, the spin-independent cross-section $\sigma_{\tilde{\chi}_1^0, N}^{\text{SI}}$ is dominated by t -channel exchange of h and h_s , with the leading contribution scaling as $\lambda^2 \kappa^2$ due to the presence of a relatively light h_s [36]. Crucially, the two exchange amplitudes can interfere destructively, producing a notable cancellation that intricately interplay among samples with different $\lambda \kappa$ values. Furthermore, with $M_1 = 150$ GeV in our analysis, the DM retains a Bino admixture up to 0.1% level. Despite being small, this component yields a non-negligible contribution for $\sigma_{\tilde{\chi}_1^0, N}^{\text{SI}}$ because the Bino-Bino-SM Higgs coupling $C_{\tilde{B}\tilde{B}H_{\text{SM}}}$ is much larger than the Singlino-Singlino-SM Higgs coupling $C_{\tilde{S}\tilde{S}H_{\text{SM}}}$ when the Higgsino mass lies around several hundred GeV. Additionally, the small \tilde{H}_d component in $\tilde{\chi}_1^0$ may also be non-negligible in the scattering since $\tilde{S} - \tilde{H}_d - H_{\text{SM}}$ coupling $C_{\tilde{S}\tilde{H}_dH_{\text{SM}}}$ is determined by λ . These effects, not previously emphasized in literature, can substantially enhance the cancellations among different contributions to $\sigma_{\tilde{\chi}_1^0, N}^{\text{SI}}$. These observations have important implications for satisfying LZ 2024 constraints: strong destructive interference permits larger $\lambda |\kappa|$ values, while weak cancellation favors smaller $\lambda |\kappa|$.

This phenomenon is numerically verified in Fig. 3, where the left and right panels display results for the h_1 and h_2 scenarios, respectively. The figure reveals that the cancellation in the h_2 scenario is significantly weaker than in the h_1 scenario, thereby favoring smaller $\lambda |\kappa|$. Nevertheless, despite this difference in cancellation strengths, both scenarios can suppress $\sigma_{\tilde{\chi}_1^0, N}^{\text{SI}}$ to values as low as 10^{-50} cm 2 . Notably, the required smallness of λ naturally aligns with constraints from Higgs data fitting, as elaborated in Section 2.2.

Finally, we examine the LHC constraints on supersymmetry. For this purpose, we project samples obtained from parameter scans and refined by LZ 2024 constraints

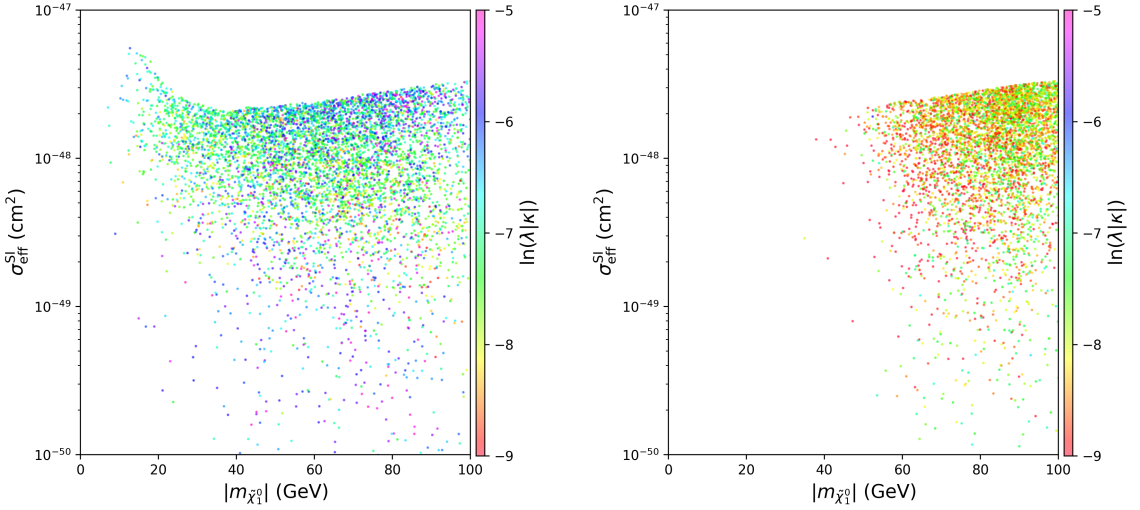


Figure 3. Scatter plots of $\sigma_{\text{eff}}^{\text{SI}}$ versus $|m_{\tilde{\chi}_1^0}|$ for the samples in the h_1 scenario (left panel) and the h_2 scenario (right panel). The color bar is defined as $\ln(\lambda|\kappa|)$, describing the coupling strength involved in the scattering.

onto $|m_{\tilde{\chi}_1^0}| - \mu_{\text{tot}}$ and $|\kappa| - \lambda$ planes, as shown in Fig. 4. Several key observations emerge:

- When the Bino-like neutralino serves as the next-to-lightest supersymmetric particle (NLSP), the decay cascades are longer and the final states have higher multiplicities (often including a light A_s), which degrades search sensitivity and relaxes the LHC bounds. In this hierarchy, i.e., $\tilde{S} < \tilde{B} < \tilde{H}$, samples with μ_{tot} as low as ~ 200 GeV remain viable, alleviating the fine-tuning in predicting Z -boson mass and preserving theoretical naturalness.
- Samples excluded by our recast are primarily characterized by final states containing three or more leptons, which fall into two categories [83]: (i) No τ leptons, at least two opposite-sign same-flavor (OSSF) lepton pairs (electrons or muons), and missing transverse momentum $p_T^{\text{miss}} \in (100, 150)$ GeV or $p_T^{\text{miss}} \geq 200$ GeV. (ii) Two τ leptons, fewer than two OSSF pairs, and $p_T^{\text{miss}} \geq 150$ GeV. Note that the substantial missing transverse momentum in these signatures constitutes a characteristic feature of supersymmetric particle production.
- The LHC and LZ 2024 constraints exhibit mutual consistency, as surviving samples display stable distributions in λ and $|\kappa|$ parameter space. Specifically, in the h_1 scenario, λ was bounded above by $\lambda \lesssim 0.048$, while $|\kappa|$ could extend up to 0.3. By contrast, the h_2 scenario imposes more stringent constraints: $\lambda \leq 0.01$ and $|\kappa| \in (0.03, 0.2)$, with most samples concentrated near $|\kappa| \simeq 0.15$.

The characteristic features of surviving samples are exemplified by two benchmark points detailed in Table 4. Both have low M_1 and μ_{tot} , and consequently the

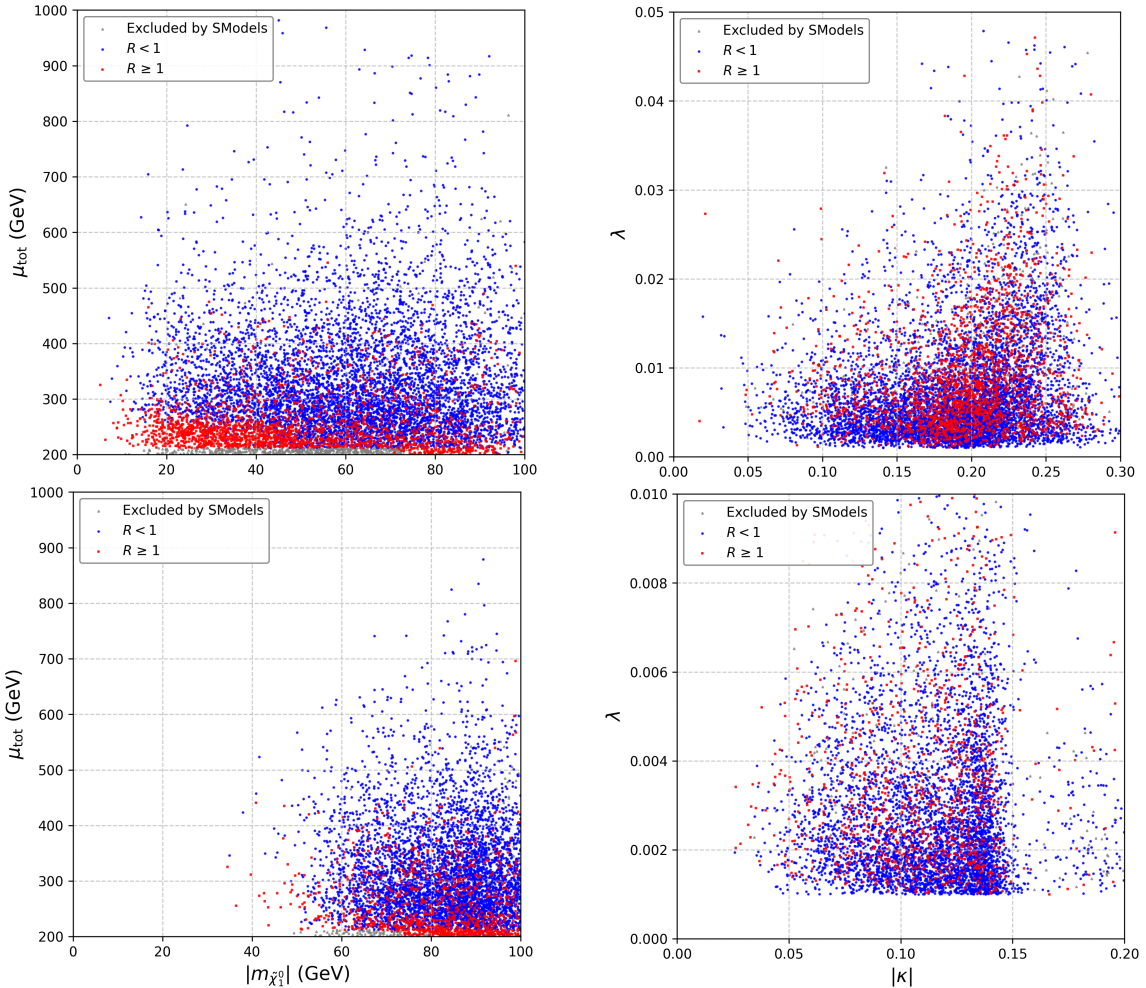


Figure 4. LHC constraints on the parameters $|m_{\tilde{\chi}_1^0}|$, μ_{tot} , $|\kappa|$, and λ . Samples include those obtained by the scans and refined by the LZ 2024 constraints. They are classified by exclusion levels, as depicted in the legend. Gray markers are excluded by SModelS-3.0.0, blue markers ($R < 1$) are consistent with all experiments, and red markers ($R \geq 1$) are excluded by LHC data. The upper panels correspond to the h_1 scenario, while the lower panels refer to the h_2 scenario.

DM acquires small but non-negligible Bino and Higgsino admixtures, especially in the h_1 case. These admixtures strengthen the destructive interference among the contributions to $\sigma_{\tilde{\chi}_1^0, N}^{\text{SI}}$, thereby suppressing the effective cross-section $\sigma_{\text{eff}}^{\text{SI}}$ below the LZ 2024 limit. In addition, the sparticle spectra yield multi-step decay chains with several competing modes (often involving a light A_s), which weakens current LHC sensitivities and allows these benchmarks to evade existing searches.

3.3 Subtleties of LHC restrictions

The results summarized in Table 3 might suggest that the LHC constraints are largely inconsequential for light DM scenarios. This impression is misleading: depending on

Table 4. Detailed information for two benchmark points aligning with all currently available experimental results, with $M_1 = 150$ GeV.

Benchmark Point BP1 (h_1 scenario)			Benchmark Point BP2 (h_2 scenario)		
λ	0.008	m_{h_s}	148.6 GeV	λ	0.002
κ	-0.194	m_h	125.4 GeV	κ	0.110
δ	0.375	m_H	1877.6 GeV	δ	0.721
$\tan \beta$	22.57	m_{A_s}	11.7 GeV	$\tan \beta$	23.88
μ	224.9 GeV	$m_{\tilde{\chi}_1^0}$	-52.4 GeV	μ	299.0 GeV
μ_{eff}	3.2 GeV	$m_{\tilde{\chi}_2^0}$	141.7 GeV	μ_{eff}	1.0 GeV
μ_{tot}	228.1 GeV	$m_{\tilde{\chi}_3^0}$	-239.0 GeV	μ_{tot}	300.0 GeV
A_λ	3275.5 GeV	$m_{\tilde{\chi}_4^0}$	244.6 GeV	A_λ	2078.0 GeV
A_κ	-288.8 GeV	$m_{\tilde{\chi}_5^0}$	2020.9 GeV	A_κ	521.3 GeV
A_t	-3846.0 GeV	$m_{\tilde{\chi}_1^\pm}$	235.0 GeV	A_t	-3546.2 GeV
M_1	150.0 GeV	$m_{\tilde{\chi}_2^\pm}$	2021.2 GeV	M_1	150.0 GeV
m_B	149.9 GeV	Ωh^2	0.122	m_B	101.5 GeV
m_C	16.7 GeV	$\sigma_{\text{eff}}^{\text{SI}}$	$2.00 \times 10^{-49} \text{ cm}^2$	m_C	19.9 GeV
m_S	-52.5 GeV	σ_n^{SD}	$4.00 \times 10^{-47} \text{ cm}^2$	m_S	-73.4 GeV
$V_{h_s}^S, V_{h_s}^{\text{SM}}, V_h^S, V_h^{\text{SM}}$			-0.999, -0.004, 0.004, -0.999	$V_{h_s}^S, V_{h_s}^{\text{SM}}, V_h^S, V_h^{\text{SM}}$	0.999, -0.025, 0.025, 0.999
$N_{11}, N_{12}, N_{13}, N_{14}, N_{15}$			-0.001, 0.000, 0.001, 0.006, -0.999	$N_{11}, N_{12}, N_{13}, N_{14}, N_{15}$	0.000, 0.000, 0.000, 0.001, -0.999
$N_{21}, N_{22}, N_{23}, N_{24}, N_{25}$			0.939, -0.008, 0.290, -0.183, -0.002	$N_{21}, N_{22}, N_{23}, N_{24}, N_{25}$	0.978, -0.004, 0.186, -0.094, 0.000
$N_{31}, N_{32}, N_{33}, N_{34}, N_{35}$			-0.077, 0.024, 0.699, 0.711, 0.005	$N_{31}, N_{32}, N_{33}, N_{34}, N_{35}$	-0.065, 0.023, 0.701, 0.710, 0.001
$N_{41}, N_{42}, N_{43}, N_{44}, N_{45}$			-0.334, -0.031, 0.654, -0.678, -0.003	$N_{41}, N_{42}, N_{43}, N_{44}, N_{45}$	-0.198, -0.033, 0.688, -0.697, 0.000
$N_{51}, N_{52}, N_{53}, N_{54}, N_{55}$			0.001, -0.999, -0.006, 0.040, 0.000	$N_{51}, N_{52}, N_{53}, N_{54}, N_{55}$	0.001, -0.999, -0.008, 0.040, 0.000
Annihilations		Fractions [%]	Annihilations		Fractions [%]
$\tilde{\chi}_1^0 \tilde{\chi}_1^0 \rightarrow A_s A_s$	99.8		$\tilde{\chi}_1^0 \tilde{\chi}_1^0 \rightarrow h_s A_s / A_s A_s$	70.0 / 30.0	
Decays		Branching ratios [%]	Decays		Branching ratios [%]
$h_s \rightarrow A_s A_s / \tilde{\chi}_1^0 \tilde{\chi}_1^0$	77.8 / 22.2		$h_s \rightarrow A_s A_s$	100.0	
$h \rightarrow A_s A_s / \tilde{\chi}_1^0 \tilde{\chi}_1^0 / \dots$	10.0 / 1.0 / ...		$h \rightarrow A_s A_s / \dots$	9.6 / ...	
$H \rightarrow b\bar{b} / \tau\bar{\tau} / \dots$	70.1 / 13.1 / ...		$H \rightarrow b\bar{b} / \tau\bar{\tau} / \dots$	71.8 / 13.4 / ...	
$A_s \rightarrow b\bar{b} / \tau\bar{\tau}$	88.8 / 9.9		$A_s \rightarrow b\bar{b} / \tau\bar{\tau}$	88.4 / 10.2	
$\tilde{\chi}_2^0 \rightarrow \tilde{\chi}_1^0 A_s$	100.0		$\tilde{\chi}_2^0 \rightarrow \tilde{\chi}_1^0 A_s$	100.0	
$\tilde{\chi}_3^0 \rightarrow \tilde{\chi}_2^0 Z$	98.1		$\tilde{\chi}_3^0 \rightarrow \tilde{\chi}_2^0 h / \tilde{\chi}_3^0 Z$	4.8 / 95.2	
$\tilde{\chi}_4^0 \rightarrow \tilde{\chi}_2^0 Z$	98.5		$\tilde{\chi}_4^0 \rightarrow \tilde{\chi}_2^0 h / \tilde{\chi}_3^0 Z$	81.2 / 18.8	
$\tilde{\chi}_5^0 \rightarrow \tilde{\chi}_3^0 h / \tilde{\chi}_3^0 Z / \tilde{\chi}_4^0 h / \tilde{\chi}_4^0 Z / \tilde{\chi}_1^\pm W^\mp$	8.2 / 15.5 / 14.7 / 7.6 / 47.6		$\tilde{\chi}_5^0 \rightarrow \tilde{\chi}_3^0 h / \tilde{\chi}_3^0 Z / \tilde{\chi}_4^0 h / \tilde{\chi}_4^0 Z / \tilde{\chi}_1^\pm W^\mp$	8.4 / 15.5 / 13.7 / 7.3 / 47.7	
$\tilde{\chi}_1^\pm \rightarrow \tilde{\chi}_2^0 W^\pm$	99.5		$\tilde{\chi}_1^\pm \rightarrow \tilde{\chi}_1^0 W^\pm$	100.0	
$\tilde{\chi}_2^\pm \rightarrow \tilde{\chi}_3^0 W^\pm / \tilde{\chi}_4^0 W^\pm / \tilde{\chi}_1^\pm h / \tilde{\chi}_1^\pm Z$	23.8 / 22.2 / 23.8 / 23.7		$\tilde{\chi}_2^\pm \rightarrow \tilde{\chi}_3^0 W^\pm / \tilde{\chi}_4^0 W^\pm / \tilde{\chi}_1^\pm h / \tilde{\chi}_1^\pm Z$	23.8 / 23.3 / 23.9 / 23.6	
R value	0.398		R value	0.295	

the sparticle mass spectrum, LHC searches can impose very strong limits on such scenarios. To illustrate this point, we now consider an alternative configuration in which the Bino is sufficiently heavy such that the sparticle spectrum exhibits the hierarchy $m_{\tilde{S}} \ll m_{\tilde{H}} \ll M_1$ ($\tilde{S} < \tilde{H} < \tilde{B}$). Compared to the previously studied configuration, this hierarchy substantially simplifies the Higgsino decay patterns, which typically strengthens the sensitivity of LHC constraints. Specifically, we repeated the analysis strategy outlined previously, fixing $M_1 = 2$ TeV. Comprehensive exploratory scans of the GNMSSM parameter space and careful examination of the acquired samples indicate that all samples with Higgsino masses below approximately 900 GeV are excluded by LHC experiments. This issue is discussed extensively below.

When characterizing light DM scenarios in the heavy Bino case, we followed the same procedure as described in Section 3.1, with the sole modification being that the Higgsino mass was scanned in the range 850 GeV to 1200 GeV. This scan initially produced 24842 samples for the h_1 scenario and 24902 samples for the h_2 scenario. After applying LZ 2024 constraints, these numbers were substantially reduced to 2885 and 139, respectively. The LHC simulation further narrowed the surviving sets

Table 5. A series of results similar to those of Table 3, but differing in two regards. 1) $M_1 = 2$ TeV. 2) In the second row of each scenario, the first numbers correspond to those further satisfying the LHC constraints (i.e., the typical $R < 1$ results), while the values inside the parentheses apply to the loose case ($R \leq 1.5$).

Scenario	Sample Size	$\tilde{\chi}_1^0 \tilde{\chi}_1^0 \rightarrow h_s h_s$	$\tilde{\chi}_1^0 \tilde{\chi}_1^0 \rightarrow A_s A_s$	$\tilde{\chi}_1^0 \tilde{\chi}_1^0 \rightarrow h_s A_s$	$\tilde{\chi}_1^0 \tilde{\chi}_1^0 \rightarrow f\bar{f}$
h_1	2885	0	97.6%	1.7%	0.6%
	1217 (2117)	0 (0)	98.4% (97.8%)	1.2% (1.7%)	0.4% (0.5%)
h_2	139	3.6%	8.6%	86.3%	1.4%
	15 (123)	0 (4.1%)	0 (8.9%)	100.0% (85.4%)	0 (1.6%)

to 1217 for the h_1 scenario and only 15 for the h_2 scenario by the nominal requirement $R < 1$. For completeness, we also adopt a loose LHC criterion $R \leq 1.5$ to account for implementation uncertainties in the recasting (see discussion below). Following this analysis strategy, we documented the updated sampling results in Table 5, where the values inside the parentheses apply to the loose case.

Compared with the $M_1 = 150$ GeV case (Table 3), significantly fewer samples satisfy the LZ 2024 constraints when $M_1 = 2$ TeV. The primary reason is that for large M_1 and μ_{tot} , the DM becomes an almost pure Singlino with negligible Bino and Higgsino admixtures. As discussed earlier, small Bino and \tilde{H}_d components are crucial for facilitating destructive interference among different contributions to $\sigma_{\tilde{\chi}_1^0 N}^{\text{SI}}$. Specifically, their markedly stronger coupling to the SM-like Higgs boson, relative to that of the Singlino, can generate sizable scattering amplitudes that interfere destructively with the pure-Singlino amplitude. When these admixtures are driven to (nearly) zero by $M_1 = 2$ TeV and $\mu_{\text{tot}} \gtrsim 900$ GeV, this interference leverage is lost and the cancellation is greatly weakened, thereby impeding effective suppression of the scattering cross-section. Consequently, most samples fail to satisfy the LZ 2024 constraints and are thus excluded even when λ is as low as 0.01. Given that this effect is particularly pronounced in the h_2 scenario, resulting in its severely limited viable sample size, we henceforth focus on the h_1 scenario.

In the heavy-Bino case, the dominant annihilation channel remains $\tilde{\chi}_1^0 \tilde{\chi}_1^0 \rightarrow A_s A_s$, with parameter-space distributions qualitatively similar to those at $M_1 = 150$ GeV but with much lower sample density. Accordingly, the physical interpretations established in the $M_1 = 150$ GeV analysis remain fully applicable, and we refrain from reiterating the detailed arguments here. One salient feature, however, warrants emphasis: the weakened cancellation among different contributions to $\sigma_{\tilde{\chi}_1^0 N}^{\text{SI}}$ causes $\sigma_{\text{eff}}^{\text{SI}}$ to be substantially elevated. As a direct consequence, surviving samples tend to cluster near the LZ 2024 exclusion boundary, and configurations with very small $\sigma_{\text{eff}}^{\text{SI}}$ are considerably rarer compared to the $M_1 = 150$ GeV case shown in Fig. 3.

On the collider side, the adjustable sparticle spectrum consists of $\tilde{\chi}_{2,3}^0$ and charginos $\tilde{\chi}_1^\pm$, with their masses approximated by $|m_{\tilde{\chi}_{2,3}^0}| \simeq m_{\tilde{\chi}_1^\pm} \simeq \mu_{\text{tot}}$, when $M_1 = 2$ TeV.

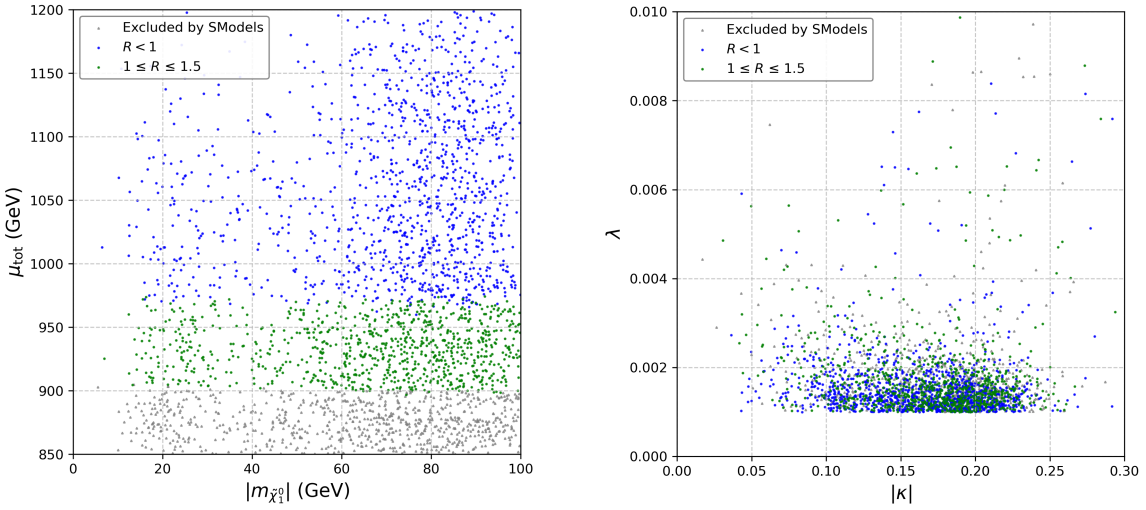


Figure 5. Similar to Fig. 4, but for $M_1 = 2$ TeV in the h_1 scenario. Samples with $R \geq 1$ are further categorized: green markers ($1 \leq R \leq 1.5$) represent those satisfying the loose LHC constraint criterion, suggesting potential compatibility with LHC data once theoretical and experimental uncertainties are properly accounted for. These uncertainties arise from multiple sources, including sparticle production cross-section calculations and involved Monte Carlo simulations.

Within the simplified mass hierarchy, the dominant decay channels for these particles are $\tilde{\chi}_{2,3}^0, \tilde{\chi}_1^\pm \rightarrow \tilde{\chi}_1^0 + W/Z/h$, as exemplified by benchmark point **BP3** in Table 6. These signatures closely resemble those targeted by the ATLAS search for charginos and neutralinos decaying to fully hadronic final states in the MSSM, as documented in Ref. [26] (ATLAS-2108-07586). Critically, in light DM scenarios, this analysis sets a lower mass limit of approximately ~ 900 GeV on the NLSP mass, as illustrated in the left panel of Fig. 5. The right panel further shows that surviving points concentrate in narrow bands, $\lambda \in (0.001, 0.01)$ and $|\kappa| \in (0.05, 0.25)$.

An important technical note concerns the $R \leq 1.5$ exclusion criterion, which was adopted to account for implementation uncertainties encountered during the recasting of the ATLAS-2108-07586 analysis into the CheckMATE-2.0.37 framework [101, 102]. Consequently, interpreting samples yielding $R \leq 1.5$ as phenomenologically consistent with current LHC experiments is justified in this context. The resulting samples with $R \leq 1.5$ are depicted by the green-shaded region in Fig. 5.

Table 6 presents two benchmark points that provide further insights. Compared to Table 4, the large μ_{tot} value produces an almost pure Singlino DM, which precludes effective cancellation among different contributions to $\sigma_{\tilde{\chi}_1^0, N}^{\text{SI}}$, leading to surviving samples with moderately large $\sigma_{\text{eff}}^{\text{SI}}$. Moreover, the simpler decay topologies in the $\tilde{S} < \tilde{H} < \tilde{B}$ hierarchy yield more detectable signatures at the LHC, resulting in notably more restrictive experimental limits.

Table 6. A list of results similar to Table 4, but with $M_1 = 2$ TeV.

Benchmark Point BP3 (h_1 scenario)				Benchmark Point BP4 (h_2 scenario)			
λ	0.001	m_{h_s}	192.1 GeV	λ	0.001	m_{h_s}	94.4 GeV
κ	0.186	m_h	125.3 GeV	κ	-0.076	m_h	125.2 GeV
δ	0.923	m_H	2550.0 GeV	δ	0.721	m_H	1677.7 GeV
$\tan \beta$	29.51	m_{A_s}	10.0 GeV	$\tan \beta$	17.89	m_{A_s}	15.7 GeV
μ	968.1 GeV	$m_{\tilde{\chi}_1^0}$	35.0 GeV	μ	967.6 GeV	$m_{\tilde{\chi}_1^0}$	-85.4 GeV
μ_{eff}	0.349 GeV	$m_{\tilde{\chi}_2^0}$	981.8 GeV	μ_{eff}	0.154 GeV	$m_{\tilde{\chi}_2^0}$	979.1 GeV
μ_{tot}	968.5 GeV	$m_{\tilde{\chi}_3^0}$	-986.7 GeV	μ_{tot}	967.8 GeV	$m_{\tilde{\chi}_3^0}$	-985.2 GeV
A_λ	2182.2 GeV	$m_{\tilde{\chi}_4^0}$	2006.6 GeV	A_λ	4923.6 GeV	$m_{\tilde{\chi}_4^0}$	2006.8 GeV
A_κ	645.3 GeV	$m_{\tilde{\chi}_5^0}$	2021.2 GeV	A_κ	-640.3 GeV	$m_{\tilde{\chi}_5^0}$	2021.3 GeV
A_t	2694.7 GeV	$m_{\tilde{\chi}_1^\pm}$	984.0 GeV	A_t	-3493.0 GeV	$m_{\tilde{\chi}_1^\pm}$	981.8 GeV
M_1	2000.0 GeV	$m_{\tilde{\chi}_2^\pm}$	2021.0 GeV	M_1	2000.0 GeV	$m_{\tilde{\chi}_2^\pm}$	2021.2 GeV
m_B	194.6 GeV	Ωh^2	0.136	m_B	96.4 GeV	Ωh^2	0.127
m_C	25.5 GeV	$\sigma_{\text{eff}}^{\text{SI}}$	$1.90 \times 10^{-48} \text{ cm}^2$	m_C	22.7 GeV	$\sigma_{\text{eff}}^{\text{SI}}$	$2.61 \times 10^{-48} \text{ cm}^2$
$m_{\tilde{S}}$	35.1 GeV	σ_n^{SD}	$3.72 \times 10^{-53} \text{ cm}^2$	$m_{\tilde{S}}$	-85.4 GeV	σ_n^{SD}	$3.93 \times 10^{-53} \text{ cm}^2$
$V_{h_s}^S, V_{h_s}^{\text{SM}}, V_h^S, V_h^{\text{SM}}$	-0.999, -0.015, 0.015, -0.999		$V_{h_s}^S, V_{h_s}^{\text{SM}}, V_h^S, V_h^{\text{SM}}$	0.999, -0.036, 0.036, 0.998			
$N_{11}, N_{12}, N_{13}, N_{14}, N_{15}$	0.000, 0.000, 0.000, 0.000, 1.000		$N_{11}, N_{12}, N_{13}, N_{14}, N_{15}$	0.000, 0.000, 0.000, 0.000, 0.999			
$N_{21}, N_{22}, N_{23}, N_{24}, N_{25}$	-0.031, 0.054, -0.707, 0.704, 0.000		$N_{21}, N_{22}, N_{23}, N_{24}, N_{25}$	-0.032, -0.056, -0.707, 0.704, 0.000			
$N_{31}, N_{32}, N_{33}, N_{34}, N_{35}$	0.010, -0.018, -0.707, -0.707, 0.000		$N_{31}, N_{32}, N_{33}, N_{34}, N_{35}$	0.010, -0.017, -0.706, -0.708, 0.000			
$N_{41}, N_{42}, N_{43}, N_{44}, N_{45}$	-0.474, -0.880, -0.016, 0.031, 0.000		$N_{41}, N_{42}, N_{43}, N_{44}, N_{45}$	-0.476, -0.879, -0.016, 0.031, 0.000			
$N_{51}, N_{52}, N_{53}, N_{54}, N_{55}$	0.880, -0.472, -0.025, 0.050, 0.000		$N_{51}, N_{52}, N_{53}, N_{54}, N_{55}$	0.879, -0.474, -0.027, 0.051, 0.000			
Annihilations	Fractions [%]		Annihilations	Fractions [%]			
$\tilde{\chi}_1^0 \tilde{\chi}_1^0 \rightarrow A_s A_s$	100.0		$\tilde{\chi}_1^0 \tilde{\chi}_1^0 \rightarrow h_s A_s / A_s A_s$	98.7 / 1.2			
Decays	Branching ratios [%]		Decays	Branching ratios [%]			
$h_s \rightarrow A_s A_s / \tilde{\chi}_1^0 \tilde{\chi}_1^0$	86.1 / 13.9		$h_s \rightarrow A_s A_s$	100.0			
$h \rightarrow A_s A_s / \dots$	10.4 / ...		$h \rightarrow A_s A_s / \dots$	8.4 / ...			
$H \rightarrow b\bar{b}/\tau\bar{\tau}$	79.6 / 19.5		$H \rightarrow b\bar{b}/\tau\bar{\tau}$	81.1 / 15.7			
$A_s \rightarrow b\bar{b}/\tau\bar{\tau}$	87.9 / 10.6		$A_s \rightarrow b\bar{b}/\tau\bar{\tau}$	89.5 / 9.6			
$\tilde{\chi}_2^0 \rightarrow \tilde{\chi}_2^0 h / \tilde{\chi}_1^0 Z$	51.7 / 47.8		$\tilde{\chi}_2^0 \rightarrow \tilde{\chi}_2^0 h / \tilde{\chi}_1^0 Z$	37.8 / 62.0			
$\tilde{\chi}_3^0 \rightarrow \tilde{\chi}_1^0 h / \tilde{\chi}_1^0 Z$	49.3 / 50.4		$\tilde{\chi}_3^0 \rightarrow \tilde{\chi}_1^0 h / \tilde{\chi}_1^0 Z$	63.5 / 36.5			
$\tilde{\chi}_4^0 \rightarrow \tilde{\chi}_2^0 h / \tilde{\chi}_3^0 Z / \tilde{\chi}_1^\pm W^\mp$	10.2 / 9.4 / 75.7		$\tilde{\chi}_4^0 \rightarrow \tilde{\chi}_2^0 h / \tilde{\chi}_3^0 Z / \tilde{\chi}_1^\pm W^\mp$	9.9 / 9.4 / 76.1			
$\tilde{\chi}_5^0 \rightarrow \tilde{\chi}_2^0 h / \tilde{\chi}_2^0 Z / \tilde{\chi}_3^0 h / \tilde{\chi}_3^0 Z$	44.2 / 4.6 / 4.6 / 42.4		$\tilde{\chi}_5^0 \rightarrow \tilde{\chi}_2^0 h / \tilde{\chi}_2^0 Z / \tilde{\chi}_3^0 h / \tilde{\chi}_3^0 Z$	43.0 / 4.1 / 4.1 / 42.4			
$\tilde{\chi}_1^\pm \rightarrow \tilde{\chi}_1^0 W^\pm$	100.0		$\tilde{\chi}_1^\pm \rightarrow \tilde{\chi}_1^0 W^\pm$	100.0			
$\tilde{\chi}_2^\pm \rightarrow \tilde{\chi}_2^0 W^\pm / \tilde{\chi}_3^0 W^\pm / \tilde{\chi}_1^\pm h / \tilde{\chi}_1^\pm Z$	23.3 / 23.4 / 24.6 / 23.4		$\tilde{\chi}_2^\pm \rightarrow \tilde{\chi}_2^0 W^\pm / \tilde{\chi}_3^0 W^\pm / \tilde{\chi}_1^\pm h / \tilde{\chi}_1^\pm Z$	23.4 / 23.7 / 24.1 / 23.7			
R value	0.963		R value	0.958			

4 Conclusion

Light supersymmetric DM with a mass of several tens of GeV warrants particular attention, as such light particles are challenging to realize within simple supersymmetric frameworks such as the MSSM or the Z_3 -NMSSM. Through a comprehensive theoretical and numerical analysis incorporating relic density, LZ 2024, Higgs data, and LHC constraints, this study establishes the GNMSSM as a robust and phenomenologically viable framework capable of naturally accommodating light supersymmetric DM. The central virtue of the GNMSSM is the effective decoupling between interactions governing thermal relic abundance and those controlling direct detection, which is enabled by allowing μ and μ' parameters to break the Z_3 symmetry of the Z_3 -NMSSM and thereby disentangle λ and κ . This feature broadens the viable parameter space and yields distinctive signatures that can help discriminate supersymmetric frameworks in future experiments. Our systemic parameter space exploration across two configurations — $M_1 = 150$ GeV and $M_1 = 2$ TeV— yields the following key insights:

- **Diverse Self-Anihilation Mechanisms:** In the h_1 scenario, DM achieves the observed relic density primarily through the $\tilde{\chi}_1^0 \tilde{\chi}_1^0 \rightarrow A_s A_s$ channel, exhibiting pronounced mass-dependent behavior across three distinct regimes. In the low-mass region ($\lesssim 30$ GeV), the t -channel dominates the annihilation process. The intermediate-mass region (30-60 GeV) features a delicate interplay between t - and s -channel contributions. In the high-mass region ($\gtrsim 60$ GeV), s -channel processes typically prevail through both resonant and non-resonant effects. In contrast, the h_2 scenario yields sufficient samples only for the $M_1 = 150$ GeV configuration, where DM achieves the correct relic density primarily via $\tilde{\chi}_1^0 \tilde{\chi}_1^0 \rightarrow h_s A_s$, with comparable s - and t -channel contributions in most parameter regions.
- **Correlation Between Direct Detection and Naturalness:** For a heavy doublet-like Higgs H , the compatibility of $\sigma_{\text{eff}}^{\text{SI}}$ with LZ 2024 constraints critically depends on the strength of destructive interference among various contributions to $\sigma_{\tilde{\chi}_1^0 N}^{\text{SI}}$. After incorporating constraints from LHC supersymmetry searches, this cancellation mechanism is substantially stronger at $M_1 = 150$ GeV than at $M_1 = 2$ TeV. Specifically, the former configuration can suppress $\sigma_{\text{eff}}^{\text{SI}}$ down to 10^{-50} cm^2 while maintaining a larger viable parameter space, thereby more readily satisfying experimental constraints. Crucially, the $M_1 = 150$ GeV configuration permits μ_{tot} values as low as ~ 200 GeV, revealing an intrinsic consistency between direct detection constraints and theoretical naturalness.
- **NLSP-Dependent LHC Constraints:** The identity of NLSP profoundly influences LHC constraints. When $M_1 = 150$ GeV, the NLSP is a Bino-dominated $\tilde{\chi}_2^0$. The resulting diverse decay modes and prolonged cascade decay chains degrade LHC search sensitivities, thereby allowing μ_{tot} values as low as ~ 200 GeV without contradicting current experimental bounds. Consequently, the model preserves extensive parameter space for future LHC exploration: in the h_1 scenario, $|m_{\tilde{\chi}_1^0}| \in (10, 100)$ GeV, $\lambda \in (0., 0.05)$, and $|\kappa| \in (0.05, 0.3)$, while in the h_2 scenario, $|m_{\tilde{\chi}_1^0}| \in (50, 100)$ GeV, $\lambda \in (0., 0.01)$, and $|\kappa| \in (0.03, 0.2)$. Both scenarios feature $m_{\tilde{\chi}_2^0} \simeq 150$ GeV. Conversely, when $M_1 = 2$ TeV, the NLSP becomes Higgsino-dominated, leading to simplified decay topologies where Higgsino-like particles decay directly to the DM. LHC experiments then impose a stringent bound of $\mu_{\text{tot}} \gtrsim 900$ GeV for such simplified signatures, substantially restricting the viable parameter space.

In summary, the GNMSSM circumvents the Z_3 -NMSSM constraint $2|\kappa| < \lambda$ in predicting Singlino-dominated DM, thereby enabling effective decoupling between DM annihilation mechanisms and DM-nucleon scattering processes. Our analysis identifies two distinct mass hierarchies within the GNMSSM: $\tilde{S} < \tilde{B} < \tilde{H}$ and $\tilde{S} <$

$\tilde{H} < \tilde{B}$, both capable of yielding phenomenologically viable DM candidates in the tens-of-GeV range. The $\tilde{S} < \tilde{B} < \tilde{H}$ hierarchy emerges as the preferred configuration, allowing μ_{tot} values as low as ~ 200 GeV and naturally accommodating Singlino-dominated light DM with proper DM relic abundance. Moreover, the presence of accompanying light particles such as A_s with characteristic LHC signatures provides additional handles for distinguishing between different supersymmetric models. By contrast, although the alternative $\tilde{S} < \tilde{H} < \tilde{B}$ hierarchy is theoretically simpler, it requires $\mu_{\text{tot}} \gtrsim 900$ GeV based on LHC constraints, resulting in approximately 0.5% fine-tuning in electroweak symmetry breaking.

By systematically exploring the previously uncharted $\tilde{S} < \tilde{B} < \tilde{H}$ parameter space, this work advances our understanding of supersymmetric DM in challenging mass regimes and provides concrete guidance for future experimental searches across multiple frontiers: direct detection experiments approaching 10^{-50} cm 2 sensitivity, collider searches for electroweakinos with complex decay chains involving light singlet states, and indirect detection through secluded-sector annihilation products. We anticipate that forthcoming experiments will provide crucial tests of the mass hierarchy identified in this study, ultimately helping to establish the correct theoretical framework for describing DM.

Acknowledgements

This work was supported by the National Natural Science Foundation of China (NNSFC) under grant No. 12575110. We thank LetPub (www letpub.com.cn) for linguistic assistance and pre-submission expert review. The authors also gratefully acknowledge the valuable discussions and insights provided by the members of the China Collaboration of Precision Testing and New Physics(CPTNP).

References

- [1] G. Jungman, M. Kamionkowski and K. Griest, *Supersymmetric dark matter*, *Phys. Rept.* **267** (1996) 195 [[hep-ph/9506380](#)].
- [2] S. Baum, M. Carena, N. R. Shah and C. E. M. Wagner, *Higgs portals for thermal Dark Matter. EFT perspectives and the NMSSM*, *JHEP* **04** (2018) 069 [[1712.09873](#)].
- [3] J. Cao, L. Meng, Y. Yue, H. Zhou and P. Zhu, *Suppressing the scattering of WIMP dark matter and nucleons in supersymmetric theories*, *Phys. Rev. D* **101** (2020) 075003 [[1910.14317](#)].
- [4] LZ collaboration, J. Aalbers et al., *Dark Matter Search Results from 4.2 Tonne-Years of Exposure of the LUX-ZEPLIN (LZ) Experiment*, *Phys. Rev. Lett.* **135** (2025) 011802 [[2410.17036](#)].

- [5] M. Pospelov, A. Ritz and M. B. Voloshin, *Secluded WIMP Dark Matter*, *Phys. Lett. B* **662** (2008) 53 [[0711.4866](#)].
- [6] C. M. Ho and R. J. Scherrer, *Limits on MeV Dark Matter from the Effective Number of Neutrinos*, *Phys. Rev. D* **87** (2013) 023505 [[1208.4347](#)].
- [7] K. Griest and M. Kamionkowski, *Unitarity Limits on the Mass and Radius of Dark Matter Particles*, *Phys. Rev. Lett.* **64** (1990) 615.
- [8] J. Smirnov and J. F. Beacom, *TeV-Scale Thermal WIMPs: Unitarity and its Consequences*, *Phys. Rev. D* **100** (2019) 043029 [[1904.11503](#)].
- [9] J. L. Feng, *Dark Matter Candidates from Particle Physics and Methods of Detection*, *Ann. Rev. Astron. Astrophys.* **48** (2010) 495 [[1003.0904](#)].
- [10] G. Arcadi, M. Dutra, P. Ghosh, M. Lindner, Y. Mambrini, M. Pierre et al., *The waning of the WIMP? A review of models, searches, and constraints*, *Eur. Phys. J. C* **78** (2018) 203 [[1703.07364](#)].
- [11] J. Abdallah et al., *Simplified Models for Dark Matter Searches at the LHC*, *Phys. Dark Univ.* **9-10** (2015) 8 [[1506.03116](#)].
- [12] A. Bottino, N. Fornengo and S. Scopel, *Light relic neutralinos*, *Phys. Rev. D* **67** (2003) 063519 [[hep-ph/0212379](#)].
- [13] A. Bottino, F. Donato, N. Fornengo and S. Scopel, *Light neutralinos and WIMP direct searches*, *Phys. Rev. D* **69** (2004) 037302 [[hep-ph/0307303](#)].
- [14] P. Belli, R. Bernabei, A. Bottino, F. Cappella, R. Cerulli, N. Fornengo et al., *Observations of annual modulation in direct detection of relic particles and light neutralinos*, *Phys. Rev. D* **84** (2011) 055014 [[1106.4667](#)].
- [15] J. F. Gunion, D. Hooper and B. McElrath, *Light neutralino dark matter in the NMSSM*, *Phys. Rev. D* **73** (2006) 015011 [[hep-ph/0509024](#)].
- [16] H. E. Haber and G. L. Kane, *The Search for Supersymmetry: Probing Physics Beyond the Standard Model*, *Phys. Rept.* **117** (1985) 75.
- [17] J. F. Gunion and H. E. Haber, *Higgs Bosons in Supersymmetric Models. 1.*, *Nucl. Phys. B* **272** (1986) 1.
- [18] U. Ellwanger, C. Hugonie and A. M. Teixeira, *The Next-to-Minimal Supersymmetric Standard Model*, *Phys. Rept.* **496** (2010) 1 [[0910.1785](#)].
- [19] D. J. Miller, R. Nevzorov and P. M. Zerwas, *The Higgs sector of the next-to-minimal supersymmetric standard model*, *Nucl. Phys. B* **681** (2004) 3 [[hep-ph/0304049](#)].
- [20] Y. He, L. Meng, Y. Yue and D. Zhang, *Impact of the recent measurement of $(g-2)\mu$, the LHC search for supersymmetry, and the LZ experiment on the minimal supersymmetric standard model*, *Phys. Rev. D* **108** (2023) 115010 [[2303.02360](#)].
- [21] P. Huang and C. E. M. Wagner, *Blind Spots for neutralino Dark Matter in the MSSM with an intermediate m_A* , *Phys. Rev. D* **90** (2014) 015018 [[1404.0392](#)].

- [22] A. Djouadi, *The Anatomy of electro-weak symmetry breaking. II. The Higgs bosons in the minimal supersymmetric model*, *Phys. Rept.* **459** (2008) 1 [[hep-ph/0503173](#)].
- [23] E. Bagnaschi et al., *Likelihood Analysis of the pMSSM11 in Light of LHC 13-TeV Data*, *Eur. Phys. J. C* **78** (2018) 256 [[1710.11091](#)].
- [24] CMS collaboration, A. Tumasyan et al., *Searches for additional Higgs bosons and for vector leptoquarks in $\tau\tau$ final states in proton-proton collisions at $\sqrt{s} = 13$ TeV*, *JHEP* **07** (2023) 073 [[2208.02717](#)].
- [25] ATLAS collaboration, G. Aad et al., *Search for chargino-neutralino pair production in final states with three leptons and missing transverse momentum in $\sqrt{s} = 13$ TeV pp collisions with the ATLAS detector*, *Eur. Phys. J. C* **81** (2021) 1118 [[2106.01676](#)].
- [26] ATLAS collaboration, G. Aad et al., *Search for charginos and neutralinos in final states with two boosted hadronically decaying bosons and missing transverse momentum in pp collisions at $\sqrt{s} = 13$ TeV with the ATLAS detector*, *Phys. Rev. D* **104** (2021) 112010 [[2108.07586](#)].
- [27] ATLAS collaboration, G. Aad et al., *Search for electroweak production of supersymmetric particles in final states with two τ -leptons in $\sqrt{s} = 13$ TeV pp collisions with the ATLAS detector*, *JHEP* **05** (2024) 150 [[2402.00603](#)].
- [28] H. Baer, V. Barger, P. Huang and X. Tata, *Natural Supersymmetry: LHC, dark matter and ILC searches*, *JHEP* **05** (2012) 109 [[1203.5539](#)].
- [29] H. Baer, V. Barger and D. Mickelson, *How conventional measures overestimate electroweak fine-tuning in supersymmetric theory*, *Phys. Rev. D* **88** (2013) 095013 [[1309.2984](#)].
- [30] J. Cao, Y. He, L. Shang, Y. Zhang and P. Zhu, *Current status of a natural NMSSM in light of LHC 13 TeV data and XENON-1T results*, *Phys. Rev. D* **99** (2019) 075020 [[1810.09143](#)].
- [31] J.-J. Cao, Z.-X. Heng, J. M. Yang, Y.-M. Zhang and J.-Y. Zhu, *A SM-like Higgs near 125 GeV in low energy SUSY: a comparative study for MSSM and NMSSM*, *JHEP* **03** (2012) 086 [[1202.5821](#)].
- [32] H. Bahl, T. Biekötter, S. Heinemeyer, C. Li, S. Paasch, G. Weiglein et al., *HiggsTools: BSM scalar phenomenology with new versions of HiggsBounds and HiggsSignals*, *Comput. Phys. Commun.* **291** (2023) 108803 [[2210.09332](#)].
- [33] J. Cao, X. Jia and J. Lian, *Unified interpretation of the muon g-2 anomaly, the 95 GeV diphoton, and bb^- excesses in the general next-to-minimal supersymmetric standard model*, *Phys. Rev. D* **110** (2024) 115039 [[2402.15847](#)].
- [34] H. Zhou, J. Cao, J. Lian and D. Zhang, *Singlino-dominated dark matter in Z3-symmetric NMSSM*, *Phys. Rev. D* **104** (2021) 015017 [[2102.05309](#)].
- [35] J. Cao, D. Li, J. Lian, Y. Yue and H. Zhou, *Singlino-dominated dark matter in general NMSSM*, *JHEP* **06** (2021) 176 [[2102.05317](#)].

- [36] L. Meng, J. Cao, F. Li and S. Yang, *Dark Matter physics in general NMSSM*, *JHEP* **08** (2024) 212 [[2405.07036](#)].
- [37] J.-J. Cao, K.-i. Hikasa, W. Wang, J. M. Yang, K.-i. Hikasa, W.-Y. Wang et al., *Light dark matter in NMSSM and implication on Higgs phenomenology*, *Phys. Lett. B* **703** (2011) 292 [[1104.1754](#)].
- [38] J. Cao, F. Ding, C. Han, J. M. Yang and J. Zhu, *A light Higgs scalar in the NMSSM confronted with the latest LHC Higgs data*, *JHEP* **11** (2013) 018 [[1309.4939](#)].
- [39] G. G. Ross and K. Schmidt-Hoberg, *The Fine-Tuning of the Generalised NMSSM*, *Nucl. Phys. B* **862** (2012) 710 [[1108.1284](#)].
- [40] S. A. Abel, *Destabilizing divergences in the NMSSM*, *Nucl. Phys. B* **480** (1996) 55 [[hep-ph/9609323](#)].
- [41] H. M. Lee, S. Raby, M. Ratz, G. G. Ross, R. Schieren, K. Schmidt-Hoberg et al., *A unique \mathbb{Z}_4^R symmetry for the MSSM*, *Phys. Lett. B* **694** (2011) 491 [[1009.0905](#)].
- [42] H. M. Lee, S. Raby, M. Ratz, G. G. Ross, R. Schieren, K. Schmidt-Hoberg et al., *Discrete R symmetries for the MSSM and its singlet extensions*, *Nucl. Phys. B* **850** (2011) 1 [[1102.3595](#)].
- [43] G. G. Ross, K. Schmidt-Hoberg and F. Staub, *The Generalised NMSSM at One Loop: Fine Tuning and Phenomenology*, *JHEP* **08** (2012) 074 [[1205.1509](#)].
- [44] U. Ellwanger, *Nonrenormalizable Interactions from Supergravity, Quantum Corrections and Effective Low-Energy Theories*, *Phys. Lett. B* **133** (1983) 187.
- [45] J. Cao, X. Jia, J. Lian and L. Meng, *95 GeV diphoton and bb^- excesses in the general next-to-minimal supersymmetric standard model*, *Phys. Rev. D* **109** (2024) 075001 [[2310.08436](#)].
- [46] W. G. Hollik, S. Liebler, G. Moortgat-Pick, S. Paßehr and G. Weiglein, *Phenomenology of the inflation-inspired NMSSM at the electroweak scale*, *Eur. Phys. J. C* **79** (2019) 75 [[1809.07371](#)].
- [47] W. G. Hollik, G. Weiglein and J. Wittbrodt, *Impact of Vacuum Stability Constraints on the Phenomenology of Supersymmetric Models*, *JHEP* **03** (2019) 109 [[1812.04644](#)].
- [48] J. Cao, X. Jia, L. Meng, Y. Yue and D. Zhang, *Status of the singlino-dominated dark matter in general Next-to-Minimal Supersymmetric Standard Model*, *JHEP* **03** (2023) 198 [[2210.08769](#)].
- [49] F. Staub, *SARAH*, [0806.0538](#).
- [50] F. Staub, *SARAH 3.2: Dirac Gauginos, UFO output, and more*, *Comput. Phys. Commun.* **184** (2013) 1792 [[1207.0906](#)].
- [51] F. Staub, *SARAH 4 : A tool for (not only SUSY) model builders*, *Comput. Phys. Commun.* **185** (2014) 1773 [[1309.7223](#)].

- [52] F. Staub, *Exploring new models in all detail with SARAH*, *Adv. High Energy Phys.* **2015** (2015) 840780 [[1503.04200](#)].
- [53] W. Porod, *SPheno, a program for calculating supersymmetric spectra, SUSY particle decays and SUSY particle production at e+ e- colliders*, *Comput. Phys. Commun.* **153** (2003) 275 [[hep-ph/0301101](#)].
- [54] W. Porod and F. Staub, *SPheno 3.1: Extensions including flavour, CP-phases and models beyond the MSSM*, *Comput. Phys. Commun.* **183** (2012) 2458 [[1104.1573](#)].
- [55] W. Porod, F. Staub and A. Vicente, *A Flavor Kit for BSM models*, *Eur. Phys. J. C* **74** (2014) 2992 [[1405.1434](#)].
- [56] G. Belanger, F. Boudjema, A. Pukhov and A. Semenov, *MicrOMEGAs: A Program for calculating the relic density in the MSSM*, *Comput. Phys. Commun.* **149** (2002) 103 [[hep-ph/0112278](#)].
- [57] G. Belanger, F. Boudjema, C. Hugonie, A. Pukhov and A. Semenov, *Relic density of dark matter in the NMSSM*, *JCAP* **09** (2005) 001 [[hep-ph/0505142](#)].
- [58] G. Belanger, F. Boudjema, A. Pukhov and A. Semenov, *MicrOMEGAs 2.0: A Program to calculate the relic density of dark matter in a generic model*, *Comput. Phys. Commun.* **176** (2007) 367 [[hep-ph/0607059](#)].
- [59] G. Belanger, F. Boudjema, A. Pukhov and A. Semenov, *micrOMEGAs: A Tool for dark matter studies*, *Nuovo Cim. C* **033N2** (2010) 111 [[1005.4133](#)].
- [60] G. Belanger, F. Boudjema, A. Pukhov and A. Semenov, *micrOMEGAs_3: A program for calculating dark matter observables*, *Comput. Phys. Commun.* **185** (2014) 960 [[1305.0237](#)].
- [61] D. Barducci, G. Belanger, J. Bernon, F. Boudjema, J. Da Silva, S. Kraml et al., *Collider limits on new physics within micrOMEGAs_4.3*, *Comput. Phys. Commun.* **222** (2018) 327 [[1606.03834](#)].
- [62] PLANCK collaboration, N. Aghanim et al., *Planck 2018 results. VI. Cosmological parameters*, *Astron. Astrophys.* **641** (2020) A6 [[1807.06209](#)].
- [63] J. Cao, Y. He, Y. Pan, Y. Yue, H. Zhou and P. Zhu, *Impact of leptonic unitarity and dark matter direct detection experiments on the NMSSM with inverse seesaw mechanism*, *JHEP* **12** (2020) 023 [[1903.01124](#)].
- [64] LZ collaboration, J. Aalbers et al., *First Dark Matter Search Results from the LUX-ZEPLIN (LZ) Experiment*, *Phys. Rev. Lett.* **131** (2023) 041002 [[2207.03764](#)].
- [65] S. Matsumoto, S. Mukhopadhyay and Y.-L. S. Tsai, *Effective Theory of WIMP Dark Matter supplemented by Simplified Models: Singlet-like Majorana fermion case*, *Phys. Rev. D* **94** (2016) 065034 [[1604.02230](#)].
- [66] P. Bechtle, S. Heinemeyer, O. Stål, T. Stefaniak and G. Weiglein, *HiggsSignals: Confronting arbitrary Higgs sectors with measurements at the Tevatron and the LHC*, *Eur. Phys. J. C* **74** (2014) 2711 [[1305.1933](#)].

- [67] O. Stål and T. Stefaniak, *Constraining extended Higgs sectors with HiggsSignals*, *PoS EPS-HEP2013* (2013) 314 [[1310.4039](#)].
- [68] P. Bechtle, S. Heinemeyer, O. Stål, T. Stefaniak and G. Weiglein, *Probing the Standard Model with Higgs signal rates from the Tevatron, the LHC and a future ILC*, *JHEP* **11** (2014) 039 [[1403.1582](#)].
- [69] P. Bechtle, S. Heinemeyer, T. Klingl, T. Stefaniak, G. Weiglein and J. Wittbrodt, *HiggsSignals-2: Probing new physics with precision Higgs measurements in the LHC 13 TeV era*, *Eur. Phys. J. C* **81** (2021) 145 [[2012.09197](#)].
- [70] P. Bechtle, O. Brein, S. Heinemeyer, G. Weiglein and K. E. Williams, *HiggsBounds: Confronting Arbitrary Higgs Sectors with Exclusion Bounds from LEP and the Tevatron*, *Comput. Phys. Commun.* **181** (2010) 138 [[0811.4169](#)].
- [71] P. Bechtle, O. Brein, S. Heinemeyer, G. Weiglein and K. E. Williams, *HiggsBounds 2.0.0: Confronting Neutral and Charged Higgs Sector Predictions with Exclusion Bounds from LEP and the Tevatron*, *Comput. Phys. Commun.* **182** (2011) 2605 [[1102.1898](#)].
- [72] P. Bechtle, O. Brein, S. Heinemeyer, O. Stål, T. Stefaniak, G. Weiglein et al., *Recent Developments in HiggsBounds and a Preview of HiggsSignals*, *PoS CHARGED2012* (2012) 024 [[1301.2345](#)].
- [73] P. Bechtle, O. Brein, S. Heinemeyer, O. Stål, T. Stefaniak, G. Weiglein et al., *HiggsBounds – 4: Improved Tests of Extended Higgs Sectors against Exclusion Bounds from LEP, the Tevatron and the LHC*, *Eur. Phys. J. C* **74** (2014) 2693 [[1311.0055](#)].
- [74] P. Bechtle, D. Dercks, S. Heinemeyer, T. Klingl, T. Stefaniak, G. Weiglein et al., *HiggsBounds-5: Testing Higgs Sectors in the LHC 13 TeV Era*, *Eur. Phys. J. C* **80** (2020) 1211 [[2006.06007](#)].
- [75] L. M. Carpenter, R. Colburn, J. Goodman and T. Linden, *Indirect Detection Constraints on s and t Channel Simplified Models of Dark Matter*, *Phys. Rev. D* **94** (2016) 055027 [[1606.04138](#)].
- [76] X.-J. Huang, C.-C. Wei, Y.-L. Wu, W.-H. Zhang and Y.-F. Zhou, *Antiprotons from dark matter annihilation through light mediators and a possible excess in AMS-02 p/p data*, *Phys. Rev. D* **95** (2017) 063021 [[1611.01983](#)].
- [77] K. K. Boddy, S. Hill, J. Kumar, P. Sandick and B. Shams Es Haghi, *MADHAT: Model-Agnostic Dark Halo Analysis Tool*, *Comput. Phys. Commun.* **261** (2021) 107815 [[1910.02890](#)].
- [78] K. K. Boddy, Z. J. Carter, J. Kumar, L. Rufino, P. Sandick and N. Tapia-Arellano, *New dark matter analysis of milky way dwarf satellite galaxies with madhatv2*, *Phys. Rev. D* **109** (2024) 103007 [[2401.05327](#)].
- [79] PARTICLE DATA GROUP collaboration, M. Tanabashi et al., *Review of Particle Physics*, *Phys. Rev. D* **98** (2018) 030001.

- [80] ATLAS collaboration, *Search for supersymmetry with two and three leptons and missing transverse momentum in the final state at $\sqrt{s}=13$ TeV with the ATLAS detector*, .
- [81] ATLAS collaboration, G. Aad et al., *Search for electroweak production of charginos and sleptons decaying into final states with two leptons and missing transverse momentum in $\sqrt{s} = 13$ TeV pp collisions using the ATLAS detector*, *Eur. Phys. J. C* **80** (2020) 123 [[1908.08215](#)].
- [82] ATLAS collaboration, M. Aaboud et al., *Search for electroweak production of supersymmetric particles in final states with two or three leptons at $\sqrt{s} = 13$ TeV with the ATLAS detector*, *Eur. Phys. J. C* **78** (2018) 995 [[1803.02762](#)].
- [83] CMS collaboration, A. M. Sirunyan et al., *Search for electroweak production of charginos and neutralinos in multilepton final states in proton-proton collisions at $\sqrt{s} = 13$ TeV*, *JHEP* **03** (2018) 166 [[1709.05406](#)].
- [84] ATLAS collaboration, *Search for chargino-neutralino production with mass splittings near the electroweak scale in three-lepton final states in $\sqrt{s} = 13$ TeV pp collisions with the ATLAS detector*, .
- [85] ATLAS collaboration, G. Aad et al., *Search for supersymmetry in events with four or more charged leptons in 139 fb^{-1} of $\sqrt{s} = 13$ TeV pp collisions with the ATLAS detector*, *JHEP* **07** (2021) 167 [[2103.11684](#)].
- [86] CMS collaboration, *Search for new physics in the compressed mass spectra scenario using events with two soft opposite-sign leptons and missing momentum energy at 13 TeV*, .
- [87] ATLAS collaboration, M. Aaboud et al., *Search for electroweak production of supersymmetric states in scenarios with compressed mass spectra at $\sqrt{s} = 13$ TeV with the ATLAS detector*, *Phys. Rev. D* **97** (2018) 052010 [[1712.08119](#)].
- [88] ATLAS collaboration, G. Aad et al., *Searches for electroweak production of supersymmetric particles with compressed mass spectra in $\sqrt{s} = 13$ TeV pp collisions with the ATLAS detector*, *Phys. Rev. D* **101** (2020) 052005 [[1911.12606](#)].
- [89] CMS collaboration, A. M. Sirunyan et al., *Search for new physics in events with two soft oppositely charged leptons and missing transverse momentum in proton-proton collisions at $\sqrt{s} = 13$ TeV*, *Phys. Lett. B* **782** (2018) 440 [[1801.01846](#)].
- [90] CMS collaboration, A. M. Sirunyan et al., *Search for supersymmetry in final states with two oppositely charged same-flavor leptons and missing transverse momentum in proton-proton collisions at $\sqrt{s} = 13$ TeV*, *JHEP* **04** (2021) 123 [[2012.08600](#)].
- [91] ATLAS collaboration, G. Aad et al., *Search for direct production of electroweakinos in final states with one lepton, missing transverse momentum and a Higgs boson decaying into two b-jets in pp collisions at $\sqrt{s} = 13$ TeV with the ATLAS detector*, *Eur. Phys. J. C* **80** (2020) 691 [[1909.09226](#)].

- [92] ATLAS collaboration, G. Aad et al., *Search for direct production of electroweakinos in final states with missing transverse momentum and a Higgs boson decaying into photons in pp collisions at $\sqrt{s} = 13$ TeV with the ATLAS detector*, *JHEP* **10** (2020) 005 [[2004.10894](#)].
- [93] ATLAS collaboration, M. Aaboud et al., *Search for photonic signatures of gauge-mediated supersymmetry in 13 TeV pp collisions with the ATLAS detector*, *Phys. Rev. D* **97** (2018) 092006 [[1802.03158](#)].
- [94] F. Feroz, M. P. Hobson and M. Bridges, *MultiNest: an efficient and robust Bayesian inference tool for cosmology and particle physics*, *Mon. Not. Roy. Astron. Soc.* **398** (2009) 1601 [[0809.3437](#)].
- [95] W. Beenakker, R. Hopker and M. Spira, *PROSPINO: A Program for the production of supersymmetric particles in next-to-leading order QCD*, [hep-ph/9611232](#).
- [96] C. K. Khosa, S. Kraml, A. Lessa, P. Neuhuber and W. Waltenberger, *SModelS Database Update v1.2.3*, *LHEP* **2020** (2020) 158 [[2005.00555](#)].
- [97] J. Alwall, M. Herquet, F. Maltoni, O. Mattelaer and T. Stelzer, *MadGraph 5 : Going Beyond*, *JHEP* **06** (2011) 128 [[1106.0522](#)].
- [98] E. Conte, B. Fuks and G. Serret, *MadAnalysis 5, A User-Friendly Framework for Collider Phenomenology*, *Comput. Phys. Commun.* **184** (2013) 222 [[1206.1599](#)].
- [99] T. Sjöstrand, S. Ask, J. R. Christiansen, R. Corke, N. Desai, P. Ilten et al., *An introduction to PYTHIA 8.2*, *Comput. Phys. Commun.* **191** (2015) 159 [[1410.3012](#)].
- [100] M. Drees, H. Dreiner, D. Schmeier, J. Tattersall and J. S. Kim, *CheckMATE: Confronting your Favourite New Physics Model with LHC Data*, *Comput. Phys. Commun.* **187** (2015) 227 [[1312.2591](#)].
- [101] D. Dercks, N. Desai, J. S. Kim, K. Rolbiecki, J. Tattersall and T. Weber, *CheckMATE 2: From the model to the limit*, *Comput. Phys. Commun.* **221** (2017) 383 [[1611.09856](#)].
- [102] J. S. Kim, D. Schmeier, J. Tattersall and K. Rolbiecki, *A framework to create customised LHC analyses within CheckMATE*, *Comput. Phys. Commun.* **196** (2015) 535 [[1503.01123](#)].
- [103] DELPHES 3 collaboration, J. de Favereau, C. Delaere, P. Demin, A. Giannanco, V. Lemaître, A. Mertens et al., *DELPHES 3, A modular framework for fast simulation of a generic collider experiment*, *JHEP* **02** (2014) 057 [[1307.6346](#)].
- [104] J. Cao, J. Lian, Y. Pan, D. Zhang and P. Zhu, *Improved $(g - 2)_\mu$ measurement and singlino dark matter in μ -term extended \mathbb{Z}_3 -NMSSM*, *JHEP* **09** (2021) 175 [[2104.03284](#)].
- [105] Z. Heng, Z. Li and H. Zhou, *Constraining the light Higgs bosons in the GNMSSM with recent Higgs data*, [2503.04023](#).

- [106] K. Griest and D. Seckel, *Three exceptions in the calculation of relic abundances*, *Phys. Rev. D* **43** (1991) 3191.